

UNIVERSIDADE FEDERAL DA INTEGRAÇÃO LATINO-AMERICANA
INSTITUTO LATINO AMERICANO DE CIÊNCIAS DA VIDA E DA NATUREZA
PROGRAMA DE PÓS-GRADUAÇÃO EM FÍSICA APLICADA

DISSERTAÇÃO DE MESTRADO

Foz do Iguaçu-Paraná

2026



UNIVERSIDADE FEDERAL DA INTEGRAÇÃO LATINO-AMERICANA
INSTITUTO LATINO AMERICANO DE CIÊNCIAS DA VIDA E DA NATUREZA
PROGRAMA DE PÓS-GRADUAÇÃO EM FÍSICA APLICADA

Broadband emission and CTAO Detectability of three Nearby Misaligned Radio Galaxies

John Esteban Mosquera Mosquera
Supervisor: Prof. Dr. Rita de Cássia dos Anjos
Co-supervisor: Dr. Rubens Pereira Costa Junior

Foz do Iguaçu-Paraná
2026

Broadband emission and CTAO Detectability of three Nearby Misaligned Radio Galaxies

John Esteban Mosquera Mosquera

Dissertação de Mestrado apresentada ao Programa de Pós-Graduação em Física Aplicada da Universidade Federal da Integração Latino-Americana (PPGFISA-UNILA) como parte dos requisitos ncessários para obtenção do título de Mestre em Física.

Orientador: Prof. Dr. Rita de Cassia dos Anjos

Coorientador: Dr. Rubens Pereira Costa Junior

Banca Examinadora

Prof. Dr. Rita de Cassia dos Anjos (Orientador)

Prof. Dr. Luiz Augusto Stuani Pereira (Membro Externo)

Prof. Dr. Alexander Arguello Quiroga (Membro Interno)

Foz do Iguaçu-Paraná

2026

Catalogação elaborada pelo Setor de Tratamento da Informação
Catalogação de Publicação na Fonte. UNILA - BIBLIOTECA LATINO-AMERICANA - CENTRAL

M912b
Mosquera, John Esteban Mosquera.
Broadband emission and CTAO Detectability of three Nearby Misaligned Radio Galaxies / John Esteban Mosquera Mosquera. - Foz do Iguaçu, 2026.
80 fls.: il.

Universidade Federal da Integração Latino-Americana, Instituto Latino-Americano de Ciências da Vida e da Natureza, Pós-Graduação en Física Aplicada.
Orientador: Prof. Dr. Rita de Cássia dos Anjos.

1. Galáxias. 2. Análise espectral. 3. Astronomia de raio gama. 4. Observatórios astronômicos. I. Anjos, Rita de Cássia dos. II. Costa Junior,

Resumo

Broadband emission and CTAO Detectability of three Nearby Misaligned Radio Galaxies

John Esteban Mosquera Mosquera

Supervisor: Prof. Dr. Rita de Cássia dos Anjos

Co-supervisor: Dr. Rubens Pereira Costa Junior

Resumo da Dissertação de Mestrado apresentada ao Programa de Pós-Graduação em Física Aplicada da Universidade Federal da Integração Latino-Americana (PPGFISA-UNILA) como parte dos requisitos necessários para obtenção do título de Mestre em Física.

Este trabalho apresenta um estudo das propriedades de emissão de banda larga e das perspectivas de detectabilidade em raios gama de muito alta energia de três radiogaláxias próximas: IC 1531, NGC 315 e PKS 2153-69, todas a uma distância $z < 0{,}03$. As distribuições espectrais de energia das fontes foram modeladas no contexto de um cenário leptônico de uma zona, utilizando o pacote *JetSeT* e dados multifrequência atualizados, compilados por meio da plataforma *Firmamento*. A componente de altas energias foi extrapolada para o regime de muito altas energias com o objetivo de avaliar a detectabilidade das fontes com o futuro Cherenkov Telescope Array Observatory (CTAO), por meio das bibliotecas *Gammapy* e *FeuPy*. Os resultados indicam que o cenário leptônico fornece uma descrição satisfatória da emissão das três fontes, embora revelem diferenças nas condições físicas das regiões emissoras. No regime de muito altas energias, IC 1531 e NGC 315 emergem como os alvos mais promissores para observações com o CTAO em exposições de 50 horas, enquanto PKS 2153-69, analisada com exposição estendida de 100 horas, apresenta perspectivas de detecção marginais.

Foz do Iguaçu-Paraná

2026

Abstract

Broadband emission and CTAO Detectability of three Nearby Misaligned Radio Galaxies

John Esteban Mosquera Mosquera

Supervisor: Prof. Dr. Rita de Cássia dos Anjos

Co-supervisor: Dr. Rubens Pereira Costa Junior

Abstract da Dissertação de Mestrado apresentada ao Programa de Pós-Graduação em Física Aplicada da Universidade Federal da Integração Latino-Americana(PPGFISA-UNILA) como parte dos requisitos necessários para obtenção do título de Mestre em Física.

This work presents a study of the broadband emission properties and the very-high-energy γ-ray detectability prospects of three nearby radio galaxies, namely IC 1531, NGC 315, and PKS 2153-69, all located at a distance $z < 0.03$. The spectral energy distributions of the sources were modeled within a one-zone leptonic scenario, using the *JetSeT* package and updated multifrequency data compiled through the *Firmamento* platform. The high-energy component was extrapolated to the very-high-energy (VHE) regime in order to assess the detectability of the sources with the upcoming Cherenkov Telescope Array Observatory (CTAO), by means of the *Gammapy* and *FeuPy* libraries. The results indicate that the leptonic scenario provides a satisfactory description of the emission of the three sources, although they reveal differences in the physical conditions of the emitting regions. In the VHE regime, IC 1531 and NGC 315 emerge as the most promising targets for CTAO observations with 50-hour exposures, while PKS 2153-69, analyzed with an extended 100-hour exposure, shows marginal detection prospects.

Foz do Iguaçu-Paraná

2026

"To my mother Rosa,
my uncles, Laureano
and Pedro Pablo,
and my aunts Zuni
and Adriana. "

Acknowledgments

I would like to express my sincere gratitude to my advisor, Prof. Rita de Cássia dos Anjos, whose guidance, patience, experience, and support were fundamental to the development of this work.

I also would like to thank my co-advisor, Dr. Rubens Pereira Costa Junior, for his valuable support and contributions throughout this research.

To my family: your unconditional love, encouragement, support, and understanding were essential pillars throughout this academic journey, and for that I am deeply grateful.

I would also like to thank UNILA and its professors, who shaped my academic trajectory. Their commitment to academic excellence provided the environment for the growth and learning that culminated in this work. I also acknowledge the financial support provided by CAPES, which was essential for the development of this research.

Finally, I thank everyone who contributed, directly or indirectly, to the completion of this thesis.

Contents

Introduction 1

1 Active Galactic Nuclei (AGNs) 5

1.1 General Properties of AGNs . . . 6

1.1.1 The Central Black Hole . . . 6

1.1.2 The Accretion Disk . . . 8

1.1.3 The Corona . . . 10

1.1.4 Broad- and Narrow-Line Regions . . . 11

1.1.5 The Dusty Torus . . . 11

1.1.6 Relativistic Jets . . . 12

1.2 Classification of AGNs . . . 13

1.2.1 Seyfert Galaxies and Quasars . . . 14

1.2.2 Blazars . . . 15

1.2.3 Radio Galaxies . . . 15

1.3 Misaligned AGNs . . . 16

1.4 Emission Mechanisms in Radio Galaxies . . . 17

1.5 Observational Signatures of Radio Galaxies . . . 18

1.6 Unified Model of AGNs . . . 19

1.7 Radio Galaxies as Multi-Messenger Sources . . . 20

2 Spectral Energy Distribution (SED) Modeling of AGNs 21

2.1 Sample Selection . . . 21

2.1.1 IC 1531 . . . 22

2.1.2 NGC 315 . . . 24

2.1.3 PKS 2153-69 . . . 26

2.2 Modeling Framework . . . 27
2.2.1 JetSeT Overview . . . 28
2.2.2 Radiative Processes . . . 28
2.3 Methodology . . . 29
2.3.1 Pre-fitting Procedure . . . 30
2.3.2 Parameter Estimation . . . 31
2.3.3 Physical Diagnostics and Derived Quantities . . . 32
2.4 Leptonic Modeling Results . . . 33
2.4.1 Initial Parameters . . . 33
2.4.2 SED Fitting Results . . . 34
2.4.3 Best-Fit Parameters . . . 37
2.4.4 Physical Interpretation . . . 40
2.5 Comparison with Previous Studies . . . 42
2.5.1 IC 1531 . . . 42
2.5.2 NGC 315 . . . 45
2.6 Summary of the Chapter . . . 46

3 Cherenkov Telescope Array (CTAO) Detectability Analysis 49
3.1 Very-high-energy (VHE) Methodology . . . 50
3.1.1 VHE Spectral Modeling with Gammapy . . . 50
3.1.2 Source Association and Counterparts . . . 51
3.1.3 Visibility Computation . . . 51
3.1.4 Detectability Criteria . . . 52
3.2 Comparative Analysis of the Three Sources . . . 52
3.2.1 Regions of Interest and Counterparts . . . 53
3.2.2 VHE Spectral Modeling . . . 55
3.2.3 Visibility from the CTAO Arrays . . . 58
3.3 Source-by-source Detectability . . . 59
3.3.1 IC 1531 . . . 59
3.3.2 NGC 315 . . . 60
3.3.3 PKS 2153-69 . . . 62
3.4 Global Discussion and Summary . . . 64

4 Conclusions and Future Work **66**

4.1 Summary of Results 66

4.2 Main Conclusions 68

4.3 Limitations of the Methodology 69

4.4 Future Work 71

A Corner plots **73**

References **76**

Introduction

Motivation and Context

Active Galactic Nuclei (AGNs) constitute one of the most luminous and energetic classes of astrophysical objects in the observable Universe. They are powered by the accretion of matter onto supermassive black holes (SMBHs) located at the centers of their host galaxies [1, 2]. Over the last few decades, these sources have been extensively studied as natural laboratories to investigate several fundamental topics in astrophysics and high-energy (HE) physics. In particular, AGNs provide valuable information about the acceleration of HE and ultra-high-energy (UHE) particles, the formation and dynamics of relativistic jets, as well as the composition and evolution of galaxies [3, 4]. Furthermore, the study of AGNs has motivated investigations of related physical processes, such as the interaction between HE particles and the Cosmic Microwave Background (CMB) [5, 6], as well as particle-antiparticle production and annihilation mechanisms relevant to multi-messenger astrophysics [7].

A particularly relevant aspect of AGN physics concerns the non-thermal broadband emission produced in relativistic jets, which extends from radio frequencies up to the very-high-energy (VHE) γ-ray regime. This radiation is commonly interpreted within leptonic or hadronic scenarios, depending on the nature of the dominant emitting particles [8, 9, 10]. Synchrotron radiation and inverse Compton (IC) scattering are usually considered the main mechanisms responsible for the characteristic double-peaked structure observed in the Spectral Energy Distributions (SEDs) of many AGNs. Modern numerical frameworks such as *JetSeT*[1] [11, 12, 13] allow for a self-consistent treatment of these processes and enable detailed modeling of the broadband emission from these objects, providing access to physically meaningful parameters such as the magnetic field strength, the bulk Lorentz factor, and the particle energy distribution [14].

[1] https://github.com/andreatramacere/jetset

In parallel with theoretical modeling efforts, the prospects for detecting AGNs in the VHE regime have become a central topic in contemporary γ-ray astrophysics [15, 16]. The Cherenkov Telescope Array Observatory (CTAO) [17] will provide unprecedented sensitivity in the energy range from a few tens of GeV up to several tens of TeV, opening a new observational window for the study of non-thermal processes in AGN jets. The combination of multiwavelength observations, leptonic modeling, and detectability analyses with CTAO represents a powerful approach to constrain the physical conditions of relativistic jets and to assess the role of misaligned AGNs as potential γ-ray and cosmic-ray emitters [18, 19, 20, 21]. Such studies are particularly relevant for nearby low-redshift sources, where the Extragalactic Background Light (EBL) absorption effects [22, 23] are reduced and the intrinsic emission can be characterized more reliably.

Objectives of the Work

In this study, we investigate the features of the SEDs of three nearby AGNs and evaluate their detection prospects with CTAO. The main goal of this thesis is to contribute to the understanding of these extragalactic sources and of the physical processes responsible for their emission across the electromagnetic spectrum, from radio frequencies up to TeV energies.

For this purpose, we selected three AGNs from the catalog presented in [24], namely IC 1531, NGC 315, and PKS 2153-69. These sources were chosen based on their redshift (z), since all of them belong to the nearby Universe ($z < 0.03$), which allows a more detailed characterization of their properties due to the larger availability of multiwavelength observational data [19, 18, 25]. In addition, these objects have been previously identified as relevant targets for studies of misaligned active galaxies and for investigations of high-energy emission processes in low-luminosity AGNs [26, 27]. The combination of SED modeling using the *JetSeT* framework with detectability analyses performed through the *Gammapy* library [28] and the *FeuPy* framework provides a comprehensive picture of the broadband emission and observational prospects of the selected sources, in connection with the catalogs and source associations available through Fermi Large Area Telescope (Fermi-LAT) data [29].

Structure of the Thesis

To provide the necessary context for this work, Chapter 1 presents a general overview of AGNs, including their main physical properties and structural components, such as the central black hole, the accretion disk, the corona, the broad- and narrow-line regions, the dusty torus, and relativistic jets. The chapter also discusses the classification of AGNs, their emission mechanisms, the observational signatures across the electromagnetic spectrum, and the unified model that links the different observed classes within a common physical framework [2, 30, 31].

Chapter 2 focuses on the modeling of the SEDs of the selected AGN sources. Initially, the sample selection criteria are presented, followed by the theoretical framework adopted for the modeling, based on a leptonic scenario. This chapter introduces the *JetSeT* code [11] and describes the main radiative processes considered in the simulations, including synchrotron emission, synchrotron self-Compton (SSC) scattering, and external Compton processes [8, 9, 10]. The methodology adopted for the fitting procedure, including pre-fitting techniques, parameter estimation, and the derivation of physical quantities, is also discussed in detail. Subsequently, each source (IC 1531, NGC 315, and PKS 2153-69) is analyzed individually, including the observational data, initial model parameters, SED fitting results, and physical interpretation of the obtained parameters. The chapter concludes with a comparison between the present results and previous studies available in the literature [19, 18, 25].

Chapter 3 presents the HE and VHE analysis of the same AGN sample, with the aim of evaluating the detectability of these sources by CTAO [17]. The methodology adopted in this chapter is based on the *Gammapy* library [28] and the *FeuPy* framework, encompassing HE spectral modeling, source association procedures, visibility calculations, and detectability criteria. The chapter also describes the construction of regions of interest (ROIs), the counterpart identification using Fermi-LAT catalogs [29], and the comparison between the modeled spectra and the CTAO sensitivity curves. For each source, the visibility conditions and detectability prospects are evaluated individually, considering observational constraints and, when applicable, absorption effects associated with the EBL [22, 23]. A global comparison and discussion of the obtained results are presented.

Finally, the thesis concludes with a summary of the main results obtained throughout this work and a discussion of the principal conclusions regarding the SED modeling and CTAO detectability of the selected AGNs. The limitations of the adopted methodology are addressed,

together with possible improvements and perspectives for future investigations involving multi-wavelength observations, more sophisticated emission models, and future CTAO observations.

Chapter 1

Active Galactic Nuclei (AGNs)

The terms "active galaxies" and "active galactic nuclei" refer to the defining feature that distinguishes these objects from inactive (normal) galaxies, namely the presence of SMBHs at their centers. These central engines are responsible for the energetic output that characterizes AGN activity and produces electromagnetic emission spanning the entire spectrum from radio frequencies up to VHE γ-rays [1, 2].

Since 2011, approximately one million AGN candidates have been identified through color selection methods, with several hundred thousand confirmed spectroscopically and having accurate redshift measurements. In the local Universe ($z \leq 0.1$), it is estimated that roughly one out of every fifty galaxies hosts a rapidly SMBHs, while about one out of every three galaxies contains a slowly accreting one [1].

Detailed studies of large samples of AGNs, as well as the understanding of their connection with inactive galaxies and their redshift evolution, began in the late 1970s, following the discovery of the first quasi-stellar objects (QSOs) in the early 1960s. Although all objects containing active SMBHs are now generally referred to as AGNs, several historical classifications originating from the 1960s and 1970s are still used in the literature, such as "Seyfert 1" and "Seyfert 2" galaxies. These classifications arose from early observational efforts to categorize sources that were later recognized to share common physical properties [1, 3].

Among the diverse AGN population, radio galaxies occupy a particularly important role in high-energy astrophysics. They are typically hosted by massive elliptical galaxies, exhibit powerful relativistic jets propagating over hundreds of kiloparsecs, and represent the parent population

of blazars within the unified model of AGNs [2, 4]. The non-thermal emission produced in their jets makes radio galaxies natural laboratories for the study of particle acceleration, multiwavelength emission processes, and, in some cases, multi-messenger phenomena. The present chapter introduces the main physical ingredients of AGNs, with particular emphasis on the structural and emission properties of radio galaxies, which constitute the focus of the analyses developed in Chapters 2 and 3.

1.1 General Properties of AGNs

AGNs are powered by accretion onto SMBHs located at the centers of galaxies. Despite their diversity in observational properties, a common structural framework has emerged, consisting of several key components, namely a central BH, an accretion disk, a hot corona, ionized gas regions, an obscuring dusty torus, and, in some cases, relativistic jets. In this section, we describe the main morphological elements of AGNs and their physical roles, with particular attention to the components most relevant for the radio-loud AGN population.

1.1.1 The Central Black Hole

At the core of every AGN lies a SMBH with masses ranging from $\sim 10^6$ to $10^{10}\,M_\odot$. In the framework of General Relativity, astrophysical BHs are fully characterized by their mass M and angular momentum. As discussed by [1], several key properties of AGNs are strongly influenced by the spin of the BH, since it determines the maximum energy that can be extracted during the accretion process.

A natural length scale associated with a BH is the gravitational radius,

$$r_g = \frac{GM}{c^2}, \tag{1.1}$$

where G is the universal gravitational constant, M is the black hole mass and c is the speed of light in a vacuum, which defines the characteristic size of the system. Rotating (Kerr) BHs exhibit a more complex spacetime structure, including an ergosphere where frame-dragging effects become important. Figure 1.1 presents both the zero spin and the Kerr BHs metrics.

The spacetime geometry around a rotating BH is described by the Kerr metric, first derived by Kerr (1963). In Boyer–Lindquist coordinates, the corresponding line element can be written

as [1]

$$ds^2 = \left(1 - \frac{2r_g r}{\Sigma}\right) c^2 dt^2 + \frac{4ar_g r \sin^2\theta}{\Sigma}\, dt\, d\phi - \frac{\Sigma}{\Delta} dr^2 - \Sigma d\theta^2 - \left(r^2 + a^2 + \frac{2r_g r a^2 \sin^2\theta}{\Sigma}\right) \sin^2\theta\, d\phi^2, \tag{1.2}$$

where

$$\Sigma = r^2 + a^2 \cos^2\theta, \tag{1.3}$$

$$\Delta = r^2 - 2r_g r + a^2, \tag{1.4}$$

and a is the dimensionless spin parameter of the BH.

The line element ds^2 is typically expressed in Boyer–Lindquist coordinates (r, θ, ϕ, t), where a represents the angular momentum per unit mass of the BH. As discussed by [31], this stationary (but not static) solution leads to several important characteristic surfaces in the spacetime geometry.

In particular, the positions of the event horizons are obtained from the condition $\Delta = 0$, yielding

$$r_{\text{horizon},\pm} = M \pm \sqrt{M^2 - a^2}, \tag{1.5}$$

while the surfaces of infinite redshift are determined from the time-time component of the metric and are given by

$$r_{\text{redshift},\pm} = M \pm \sqrt{M^2 - a^2 \cos^2\theta}. \tag{1.6}$$

The region between the outer event horizon and the outer redshift surface defines the ergosphere, where frame-dragging effects become significant and rotational energy can be extracted from the BH. This extraction mechanism plays a particularly important role in the context of radio-loud AGNs, since it is widely considered the most likely engine powering the relativistic jets observed in radio galaxies and blazars [4, 14].

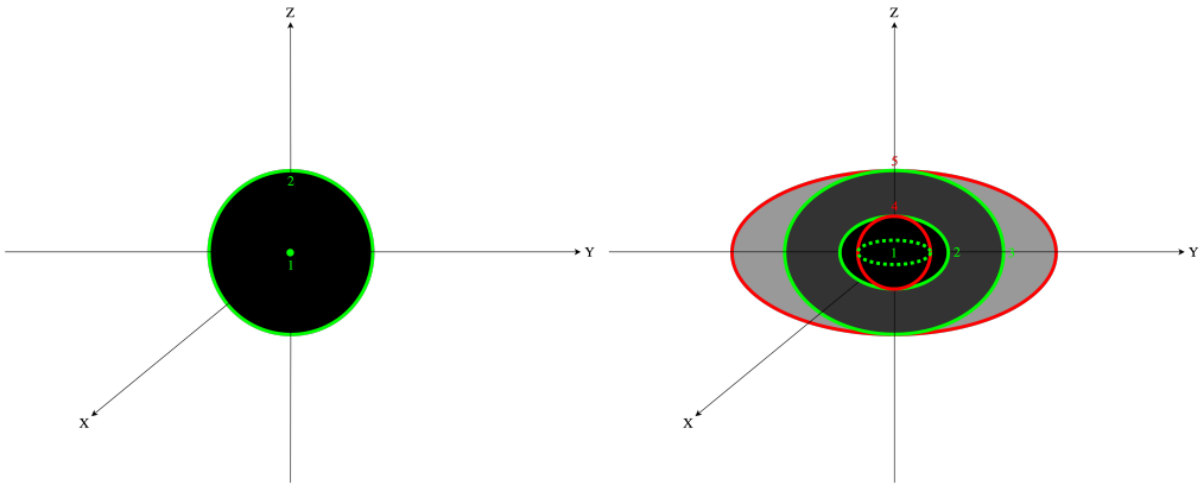

Figure 1.1: Simplified comparison of Black Holes (BHs) as described by different metrics taken from [31]. The left panel displays a zero spin BH event horizon (2) as described by the Schwarzschild metric with a mathematical point-like singularity (1). The right panel displays a BH as described by the Kerr metric. The ring-like singularity (1) is surrounded by the inner surface of infinite redshift (4) followed by the inner event horizon (2). (3) highlights the outer event horizon which is the inner border of the ergosphere, shown in light grey within the outer surface of infinite redshift (5).

In the special case of a non-rotating BH ($a = 0$), the location of the event horizon reduces to the Schwarzschild solution with $r_s = 2r_g$. The spin of the BH plays a crucial role in AGN physics, influencing both the inner structure of the accretion flow and the efficiency of energy conversion. In particular, the radiative efficiency of thin-disk accretion can vary by up to an order of magnitude between non-rotating and maximally rotating BHs, highlighting the importance of spin in determining the energetics of AGN systems [1].

1.1.2 The Accretion Disk

Matter falling toward the BH forms an accretion disk as a consequence of angular momentum conservation. As described by [31], infalling gas initially approaches the BH from different directions, but dissipative processes and rotation lead to the formation of a flattened structure in which gravitational and centrifugal forces are balanced. In this configuration, the disk follows a Keplerian rotation profile.

In the Keplerian approximation, the azimuthal velocity v_ϕ of the disk material at a distance

r from the BH is given by

$$v_\phi = \sqrt{\frac{GM}{r}}. \tag{1.7}$$

The inner edge of the accretion disk is determined by the innermost stable circular orbit (ISCO), whose location depends strongly on the BH spin.

The gravitational energy released during accretion is converted into radiation through viscous dissipation within the disk. This process heats the plasma and leads to a multi-temperature structure, where the temperature decreases with increasing radial distance. In a simplified description, as it is shown in Figure 1.2, the disk emission can be approximated as the superposition of blackbody spectra originating from different radii, producing the characteristic optical and ultraviolet emission observed in many AGNs. The radial dependence of the disk temperature can be approximated as [31]

$$T(r) \propto \dot{M}^{1/4} M^{-1/2} \left(\frac{r}{R_S}\right)^{-3/4}, \tag{1.8}$$

where $\dot{M}$ is the mass accretion rate and R_S is the Schwarzschild radius.

The maximum luminosity that can be sustained under steady accretion is given by the Eddington luminosity [1],

$$L_{\rm Edd} \approx 1.3 \times 10^{38} \left(\frac{M}{M_\odot}\right) \,{\rm erg\,s^{-1}}. \tag{1.9}$$

Including the radiative efficiency η, the dimensionless accretion rate is expressed as [31]

$$\dot{m} = \frac{\eta \dot{M} c^2}{L_{\rm Edd}} = \frac{\dot{M}}{\dot{M}_{\rm Edd}}, \tag{1.10}$$

where $\dot{M}_{\rm Edd}$ is the Eddington accretion rate. Observationally, AGNs span a wide range of accretion regimes, from very low accretion rates ($\dot{m} \ll 10^{-6}$), characteristic of quiescent systems and of low-luminosity AGNs such as several Fanaroff-Riley type I (FR I) radio galaxies, to high accretion states ($\dot{m} \gtrsim 10^{-1}$), where thermal emission from the disk dominates and a standard radiatively efficient disk develops [4, 18].

In magnetized configurations, the accretion process can also contribute to the launching of relativistic jets through mechanisms such as the Blandford-Znajek process or the development of magnetically arrested disks (MAD). The MAD scenario is particularly relevant for radio-loud AGNs, where strong large-scale magnetic fields concentrated near the BH horizon are believed to enable efficient extraction of rotational energy and to sustain the powerful jets observed in radio galaxies [4].

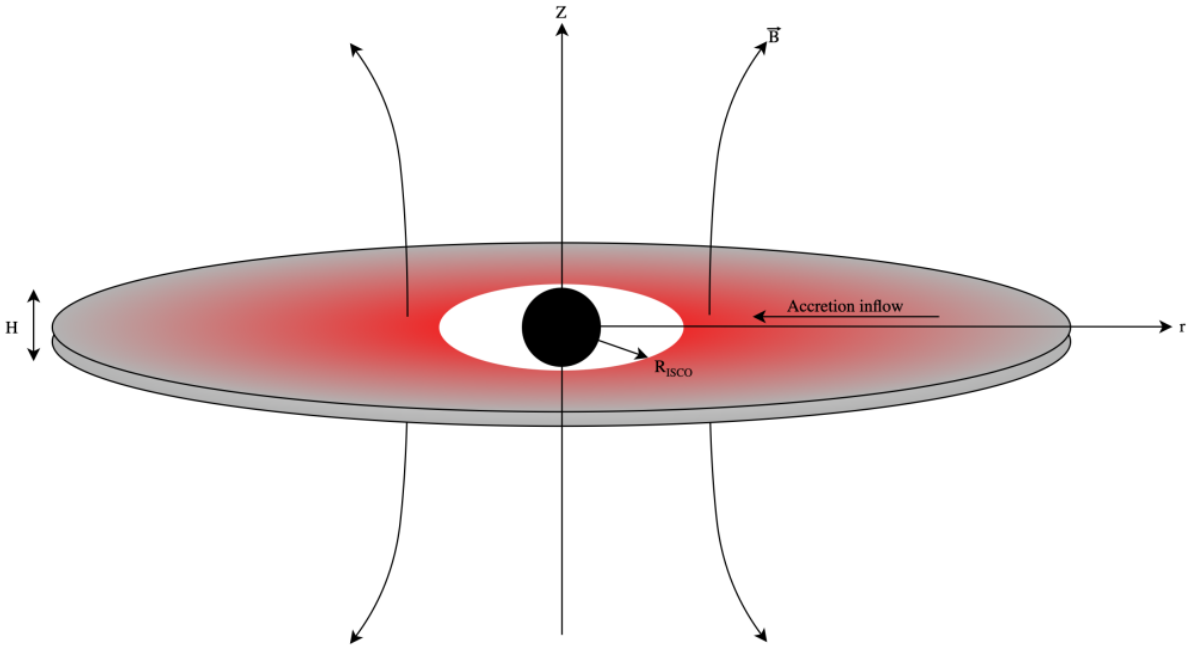

Figure 1.2: Representation of a magnetically arrested disk (MAD) from [31]. The red color gradient represents the decreasing temperature in the radial direction, where H is the disk scale height and R_{ISCO} is the radius of the Innermost Stable Circular Orbit (ISCO), and $\vec{B}$ denotes the poloidal magnetic field lines.

1.1.3 The Corona

Above and below the accretion disk, a hot, optically thin plasma known as the corona is commonly observed. As discussed by [31], this region is characterized by typical temperatures of $T \sim 10^7$–10^8 K and is responsible for the X-ray emission in AGNs.

The corona interacts with the radiation emitted by the disk, reprocessing low-energy photons into higher energies through IC scattering. Part of this high-energy radiation is directed back toward the disk, leading to reflection features in the observed spectra. As highlighted in [31], the disk-corona system therefore plays a central role in shaping the high-energy emission of AGNs. In low-luminosity radio galaxies, where the standard thin disk may be replaced by a radiatively inefficient accretion flow, the corona and the disk are not always clearly distinguishable, and the inner accretion structure is often interpreted as a hot, geometrically thick flow [18, 26].

1.1.4 Broad- and Narrow-Line Regions

Surrounding the central engine are regions of ionized gas that produce the characteristic emission lines observed in AGN spectra. In [1], these regions are commonly divided into the broad-line region (BLR) and the narrow-line region (NLR), based on their physical properties and emission line profiles.

The BLR is located at distances of $\sim 10^{-2}$–1 pc from the BH and consists of dense clouds moving at high velocities. These motions result in Doppler-broadened emission lines, with widths corresponding to velocities of up to $\sim 10^4$ km s^{-1} [1]. At larger distances, typically from a few parsecs to kiloparsec scales, lies the NLR. In this region, the gas density is lower, and the velocities are smaller, producing narrower emission lines. The ionization of both regions is primarily driven by the radiation field originating from the accretion disk and corona [1].

In the context of radio galaxies, the strength of the optical and ultraviolet emission lines, particularly the high-excitation lines associated with the BLR, is often used to separate high-excitation radio galaxies (HERGs) from low-excitation radio galaxies (LERGs), a distinction that reflects different accretion modes and is discussed in Section 1.2 [4].

1.1.5 The Dusty Torus

Encircling the inner regions of the AGN, a geometrically thick structure composed of gas and dust is commonly referred to as the torus. In [31], this component is located at parsec-scale distances and is characterized by high column densities, making it optically thick at optical and ultraviolet wavelengths.

Dust within the torus absorbs high-energy radiation from the central engine and re-emits it in the infrared, thereby contributing significantly to the infrared component of the SED. The torus therefore plays an important role in the energy balance of AGNs. Modern models suggest that the torus is not a continuous medium but rather composed of discrete clouds, forming a clumpy structure. As discussed in [31], this geometry leads to a probabilistic obscuration of the central engine and provides a natural explanation for the observed similarities between different AGN classes, particularly in the infrared. In low-luminosity radio galaxies, the infrared excess associated with the torus tends to be weak or absent, supporting the view that some FR I sources lack a fully developed dust torus [4, 18].

1.1.6 Relativistic Jets

Relativistic jets are among the most distinctive features of AGNs and constitute the defining ingredient of the radio-loud population. These collimated outflows are believed to originate from the vicinity of the BH and the inner accretion flow and propagate at relativistic speeds along the rotational axis of the system, transporting energy from sub-parsec scales up to distances of hundreds of kiloparsecs [4, 14].

The launching mechanism of relativistic jets is commonly attributed to the extraction of rotational energy from the central BH through the Blandford-Znajek process, or to the magnetohydrodynamic acceleration of plasma from the inner accretion disk. Both mechanisms require the presence of strong, large-scale magnetic fields anchored close to the BH, conditions that are naturally produced in magnetically arrested disk configurations [4].

The emission from AGN jets is generally interpreted within leptonic or hadronic scenarios, depending on the nature of the radiating particles [8, 9, 10]. In purely leptonic models, the high-energy emission is produced by relativistic electrons through synchrotron radiation and IC processes. However, in several well-studied sources, leptonic models alone may not fully account for the observed γ-ray luminosity, motivating the consideration of hybrid scenarios that include relativistic hadrons. Hadronic and lepto-hadronic models are particularly relevant in the context of multi-messenger astrophysics, where AGN jets are considered candidate sources of ultra-high-energy cosmic rays (UHECRs) and astrophysical neutrinos [20, 21, 16].

A key aspect of jet emission is its strong variability, particularly in the γ-ray regime. Rapid variability implies that the emitting region must be compact. Under such conditions, high-energy photons are expected to interact with lower-energy photons, leading to electron-positron pair production. As noted by [1], this would make the region highly opaque unless the emission is strongly beamed. The relativistic motion of the jet, combined with Doppler boosting, allows photons to propagate in a narrow cone, effectively reducing the opacity and enabling the escape of high-energy radiation. The amount of beaming is quantified by the Doppler factor $\delta = [\Gamma(1 - \beta\cos\theta)]^{-1}$, where Γ is the bulk Lorentz factor of the jet, $\beta = v/c$, and θ is the angle between the jet axis and the line of sight. In blazars, where θ is small, δ can reach values of several tens, while in misaligned radio galaxies δ is typically of order a few, leading to much weaker apparent emission [2, 4].

Observationally, jets are detected across a wide range of wavelengths. In addition to radio emission, many AGNs exhibit extended jet structures in X-rays, and in some cases also in the

optical band. These multiwavelength observations provide direct evidence for the presence of relativistic particles and ongoing energy transport over kiloparsec scales, and they are particularly well documented in nearby radio galaxies such as M87, Centaurus A, NGC 315, and PKS 2153-69 [26, 25, 27].

In this work, the jet emission of the selected sources is modeled within a one-zone leptonic framework, where a compact region of relativistic electrons is responsible for both synchrotron and IC radiation. This approach, implemented through the *JetSeT* numerical framework [11, 12, 13], provides a self-consistent description of the broadband SED while capturing the main physical processes governing the observed emission.

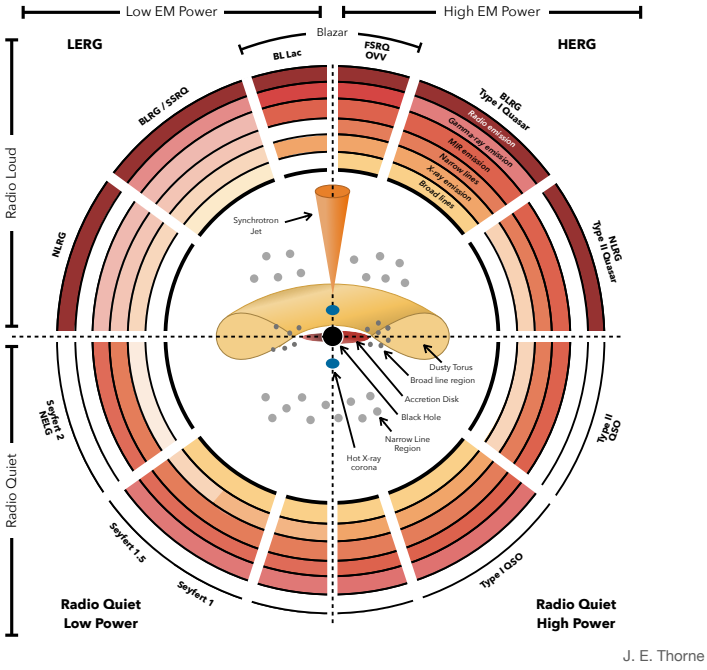

Figure 1.3: AGN unification scheme from [30]. The AGN classes are split into four quadrants. From left to right they can be sorted by emission power and from top to bottom by the appearance of a jet distinguished by their radio-loudness. In the radial direction, the unification scheme highlights the AGN classes distinguished by their orientation angle.

1.2 Classification of AGNs

Throughout history, AGNs have been classified according to different observational properties, reflecting the context in which they were discovered. As presented by [1, 3], these extra-

galactic sources can be organized based on three main criteria, namely their radio emission, their luminosity, and their orientation with respect to the observer.

The first criterion separates AGNs into radio-loud and radio-quiet sources. Radio-loud AGNs exhibit strong emission in the radio band, typically associated with the presence of relativistic jets, whereas radio-quiet AGNs show comparatively weaker radio emission. The radio-loud population, despite representing only about 10% of the total AGN population, plays a dominant role in high-energy astrophysics, since virtually all γ-ray-detected AGNs belong to this class [4, 3].

The second criterion divides AGNs into low- and high-luminosity objects. Seyfert galaxies are generally associated with lower luminosities, while quasars represent the most luminous members of the AGN population. The third criterion relates the observed properties to the viewing angle of the system. According to the unified model [2], differences between various classes of AGNs can be largely explained by orientation effects with respect to the relativistic jet and to the obscuring torus. In what follows, the main observational classes are briefly reviewed, with a more detailed discussion devoted to radio galaxies, which constitute the focus of this work.

1.2.1 Seyfert Galaxies and Quasars

Seyfert galaxies are among the most common types of AGNs and are typically found in spiral galaxies at relatively low redshift. They are characterized by bright nuclei and strong emission lines superimposed on the spectrum of the host galaxy. Based on their optical spectra, Seyfert galaxies are divided into two main classes, namely Seyfert 1 and Seyfert 2. Seyfert 1 galaxies exhibit both narrow and broad emission lines, while Seyfert 2 galaxies display only narrow emission lines. This difference is commonly interpreted within the unified model, where the BLR in Seyfert 2 galaxies is obscured by the dusty torus along the line of sight. Seyfert galaxies are generally considered low- to intermediate-luminosity AGNs and are predominantly radio-quiet, although some weak radio emission may be present.

QSOs represent the most luminous class of AGNs and were initially identified due to their star-like appearance in optical images combined with strong emission lines at high redshift. Their bolometric luminosity can exceed that of the entire host galaxy, often surpassing 10^{45} erg s^{-1}, making them visible across cosmological distances. Depending on their radio emission, quasars can be further divided into radio-loud and radio-quiet subclasses. Radio-loud quasars are associated with powerful relativistic jets, while radio-quiet quasars lack prominent jet activity [1, 3].

Since the present work focuses on radio-loud AGNs observed at large viewing angles, Seyfert galaxies and radio-quiet quasars are not addressed in further detail and are mentioned here only as part of the broader AGN classification framework.

1.2.2 Blazars

Blazars correspond to radio-loud AGNs whose relativistic jets are oriented close to the line of sight, typically within a few degrees of the jet axis. As a consequence, their emission is strongly affected by relativistic beaming, leading to enhanced apparent luminosity, rapid variability across the electromagnetic spectrum, and a dominant non-thermal continuum extending from radio to VHE γ-rays [8, 9]. Blazars are conventionally divided into BL Lacertae objects (BL Lacs) and flat-spectrum radio quasars (FSRQs), depending on the strength of their optical emission lines.

Although blazars constitute only a small fraction of the AGN population, they dominate the extragalactic γ-ray sky and have been extensively studied as candidate sources of UHECRs and astrophysical neutrinos [7, 20, 21, 16]. In the unified picture, blazars and radio galaxies represent the same physical class of objects observed from different angles, with blazars corresponding to small viewing angles and radio galaxies to large ones.

1.2.3 Radio Galaxies

Radio galaxies are radio-loud AGNs whose relativistic jets are oriented at large angles relative to the line of sight. They are typically hosted by massive elliptical galaxies and are predominantly found at low to intermediate redshifts. Their defining characteristic is the presence of large-scale relativistic jets that propagate from the central engine into the surrounding intergalactic medium, often producing extended radio structures such as lobes and hot spots [4].

The most widely used morphological classification of radio galaxies is the Fanaroff-Riley scheme, which divides these sources into two main types based on the spatial distribution of their radio brightness. FR I radio galaxies exhibit jets that are brightest near the core and fade with distance, indicating gradual deceleration of the jet as it interacts with the surrounding medium. They are typically associated with lower radio luminosities and are commonly found in low-luminosity AGNs (LLAGNs). In contrast, Fanaroff-Riley type II (FR II) radio galaxies

display bright hot spots at the edges of their radio lobes, suggesting more powerful and well-collimated jets that remain relativistic up to large distances from the central engine. These sources are typically associated with higher radio luminosities and stronger emission lines [4].

In addition to the FR morphological classification, radio galaxies are also commonly separated according to the excitation level of their optical emission lines. HERGs display strong, narrow high-ionization lines and are interpreted as systems with a radiatively efficient accretion flow, while LERGs exhibit weak optical emission lines and are typically associated with low accretion rates and radiatively inefficient accretion flows. Most FR I sources are LERGs, while FR II radio galaxies include both LERGs and HERGs [4, 18].

Radio galaxies are particularly important for the study of non-thermal emission processes, as their jets are efficient sites of particle acceleration over a wide range of spatial scales [14]. The acceleration mechanisms invoked in these environments include diffusive shock acceleration, magnetic reconnection, and shear acceleration in stratified jet structures. The accelerated particles radiate over the entire electromagnetic spectrum, producing the characteristic broadband emission used in SED modeling.

The three sources analyzed in this work, namely IC 1531, NGC 315, and PKS 2153-69, are all classified as radio galaxies in the nearby Universe. IC 1531 and NGC 315 are FR I radio galaxies, the latter being one of the largest and best-studied nearby giant radio galaxies, while PKS 2153-69 is a FR II radio galaxy exhibiting prominent jet-cloud interactions and well-defined radio lobes [19, 26, 25, 27]. These sources will be discussed in detail in Chapter 2.

1.3 Misaligned AGNs

The term misaligned AGNs (MAGNs) refers to radio-loud AGNs whose relativistic jets are oriented at angles larger than $\sim 10^{\circ}$ with respect to the line of sight. Within the unified model, MAGNs are interpreted as the parent population of blazars, observed from off-axis directions [2, 4]. Most radio galaxies, including IC 1531, NGC 315, and PKS 2153-69, fall into this category.

The interest in MAGNs has grown substantially after the detection of several of these sources in the HE γ-ray regime by the Fermi-LAT. The Fermi-LAT fourth source catalog includes a small but increasing number of misaligned AGNs as significant γ-ray emitters [29], providing a unique opportunity to study particle acceleration and high-energy emission processes in regimes where

relativistic boosting is moderate. In contrast to blazars, where the strong Doppler enhancement dominates the observed emission, the broadband emission of MAGNs is more representative of the intrinsic properties of the jet, making these sources valuable laboratories for testing emission models.

In the VHE regime, however, the detection of MAGNs has remained challenging. Only a handful of misaligned AGNs have been firmly established as TeV emitters by current imaging atmospheric Cherenkov telescopes, including M87, Centaurus A, NGC 1275, IC 310, and 3C 264. The moderate Doppler factors characteristic of MAGNs reduce the apparent flux at TeV energies, often placing it close to or below the sensitivity of present-day instruments. This motivates dedicated detectability studies for the next-generation CTAO [17], which is expected to provide unprecedented sensitivity in the energy range from a few tens of GeV up to several tens of TeV. The detectability assessment of nearby MAGNs with CTAO constitutes the central goal of Chapter 3.

1.4 Emission Mechanisms in Radio Galaxies

Radio galaxies emit radiation across the entire electromagnetic spectrum, from radio frequencies up to VHE γ-rays. This broadband emission arises from a combination of thermal and non-thermal processes occurring in different regions of the system, including the accretion flow, the surrounding gas, and, most importantly for radio-loud sources, the relativistic jets [1, 4].

Thermal emission is primarily associated with the accretion disk and, in luminous radio galaxies, with the dusty torus. In the standard thin-disk model, gravitational energy released during accretion is efficiently converted into radiation, producing a multi-temperature blackbody spectrum that typically peaks in the optical-ultraviolet range [1]. In low-luminosity radio galaxies, however, the disk is often radiatively inefficient and the optical-ultraviolet continuum is weak, with the SED being dominated by non-thermal emission from the jet [18, 26].

Non-thermal emission dominates in radio-loud AGNs and is generally attributed to relativistic jets. In these environments, charged particles are accelerated to high energies and radiate through synchrotron emission as they spiral around magnetic field lines. This process produces broadband emission extending from radio frequencies up to optical or X-ray energies and constitutes the low-energy component of the characteristic double-peaked SED [9].

At higher energies, IC scattering becomes the dominant emission mechanism, whereby relativistic electrons transfer energy to low-energy photons, boosting them to X-ray and γ-ray energies. When the seed photons originate from synchrotron emission within the jet, the process is referred to as SSC, whereas if the photons are external to the jet, originating from regions such as the accretion disk, the BLR, or the dusty torus, the process is known as external Compton (EC) [9, 11]. In the case of low-luminosity radio galaxies, the relatively weak external photon fields make SSC the most natural mechanism to describe the high-energy emission, an approach adopted in the modeling presented in Chapter 2.

In addition to leptonic processes, hadronic mechanisms may also contribute to the high-energy emission. These include proton synchrotron radiation and photohadronic interactions, where relativistic protons interact with ambient photon fields to produce secondary particles such as pions, which subsequently decay into γ-rays and neutrinos [8, 10]. Although hadronic processes are generally less efficient than leptonic ones in reproducing the bulk of the observed emission, they are of particular interest in the context of multi-messenger astrophysics and have been invoked to explain hard γ-ray spectra in specific sources [20, 21, 16].

The interplay between these radiative processes results in the characteristic double-peaked structure observed in the SEDs of radio galaxies and blazars. The low-energy peak is typically associated with synchrotron emission, while the high-energy peak is commonly attributed to IC scattering in leptonic models or to hadronic interactions in more complex scenarios [1, 9].

1.5 Observational Signatures of Radio Galaxies

The physical processes occurring in radio galaxies manifest through a variety of observable features over different wavelengths. These observational signatures provide essential information for constraining theoretical models and for testing the unified scheme of AGNs presented in Figure 1.3.

The most distinctive feature of radio galaxies is their non-thermal broadband emission, which extends from radio frequencies up to γ-rays and is well represented through SEDs. The morphology observed in the radio band provides direct evidence of the presence and dynamics of relativistic jets, including features such as the core, the jet itself, hot spots, and extended radio lobes [4].

X-ray observations of radio galaxies, performed with instruments such as *Chandra* [32], *XMM-Newton* [33], and *NuSTAR* [34], reveal a combination of nuclear emission, jet-related emission, and, in some cases, signatures of hot gas in the host environment. In low-luminosity radio galaxies, the nuclear X-ray emission has been used to test the presence of radiatively inefficient accretion flows and to constrain the inner accretion structure [26, 18].

In the γ-ray band, observations with the *Fermi-LAT* [35] have established a small population of MAGNs as significant HE emitters. The Fermi-LAT fourth source catalog [29] provides flux measurements, spectral indices, and source associations that constitute the main observational input for the HE modeling described in Chapter 3. In addition, multiwavelength observations are essential to reconstruct the full SED and to disentangle the contributions of different emission components. Variability is also a defining property of AGN jets, and it provides important constraints on the size and energetics of the emitting region.

1.6 Unified Model of AGNs

The diversity of observational properties exhibited by AGNs can be understood within the framework of the unified model. According to this model, the different classes of AGNs do not correspond to intrinsically distinct types of objects, but rather to the same physical system observed under different conditions, particularly orientation and obscuration [2]. In its simplest form, the unified model describes an AGN as a system composed of a SMBH surrounded by an accretion disk, the BLR and NLR, and a dusty torus. In radio-loud sources, relativistic jets are also present, extending from the central region to large distances.

A key element of the unified model is the presence of the obscuring torus. When the line of sight to the observer is unobstructed, the central engine and the BLR are directly visible, and the source is classified as a type-I AGN. In contrast, when the torus obscures the central region, only the narrow-line emission is observed, leading to a type-II classification. This interpretation naturally explains the differences between Seyfert 1 and Seyfert 2 galaxies.

Orientation also plays a fundamental role in radio-loud AGNs. When the relativistic jet is aligned close to the line of sight, relativistic effects such as Doppler boosting strongly enhance the observed emission, and the source appears as a blazar. When the jet is observed at larger angles, the same intrinsic object is classified as a radio galaxy or, more specifically, as a MAGN. Within

this framework, the three sources analyzed in this work can be regarded as off-axis counterparts of the blazar population, which makes them particularly interesting for probing the intrinsic emission of relativistic jets without the dominant influence of strong Doppler boosting [4, 18].

1.7 Radio Galaxies as Multi-Messenger Sources

The role of AGNs in multi-messenger astrophysics has become increasingly important after the detection of high-energy astrophysical neutrinos by the IceCube observatory and the multi-messenger association between IceCube-170922A and the blazar TXS 0506+056 [7]. Radio galaxies, despite being weaker γ-ray emitters than blazars, have been proposed as plausible sources of UHECRs, thanks to their powerful jets, extended radio lobes, and large reservoirs of magnetized plasma capable of accelerating protons and heavier nuclei to extreme energies [20, 21, 16].

The propagation of UHECRs over cosmological distances is limited by interactions with the CMB, leading to the well-known Greisen-Zatsepin-Kuzmin (GZK) cutoff [5, 6]. As a consequence, the sources of the highest-energy cosmic rays are expected to be located within a few hundred megaparsecs from the Earth, a volume that includes a significant population of nearby radio galaxies. This makes nearby low-redshift radio galaxies, such as the ones analyzed in this work, particularly relevant for multi-messenger studies.

The combination of SED modeling and VHE detectability analyses, as carried out in Chapters 2 and 3, provides a powerful approach to investigate the role of nearby radio galaxies as candidate sources of HE photons, UHECRs, and astrophysical neutrinos. The expected sensitivity of the CTAO [17], combined with the spectral information available from the Fermi-LAT [29] and other multiwavelength facilities, will allow significant progress in this direction over the coming years.

Chapter 2

Spectral Energy Distribution (SED) Modeling of AGNs

SED modeling of three nearby radio galaxies, namely IC 1531, NGC 315, and PKS 2153-69, all selected from the catalog of [24] on the basis of their low redshift ($z < 0.03$). Their proximity allows for a more reliable construction of the SED, as multiwavelength observational data are more abundant and the properties of the host galaxies can be characterized in greater detail. The modeling is carried out within a one-zone leptonic framework using the *JetSeT* numerical package [11, 12, 13], with the goal of constraining the physical conditions of the jets and providing the spectral input for the very-high-energy detectability analysis developed in Chapter 3.

The chapter is organized as follows. Section 2.1 describes the selected sample, including a detailed presentation of each source. Section 2.2 introduces the theoretical framework adopted for the modeling. Section 2.3 discusses the methodology used in the fitting procedure. Section 2.4 presents the modeling results, including initial parameters, best-fit values, and the physical interpretation for each source. Section 2.5 compares the obtained results with previous studies available in the literature. Finally, Section 2.6 summarizes the main findings of the chapter and outlines the connection with the very-high-energy analysis developed in Chapter 3.

2.1 Sample Selection

The sample analyzed in this work consists of three nearby radio galaxies, all classified as misaligned active galactic nuclei (MAGNs). The selection was based on three main criteria, namely a redshift $z < 0.03$, the availability of broadband multiwavelength observational data, and a relevant role for the study of non-thermal emission processes in relativistic jets. Within the Fanaroff-Riley classification, two of the selected sources (IC 1531 and NGC 315) are classified as FR I radio galaxies, while PKS 2153-69 is a FR II radio galaxy, allowing a comparative analysis of the SED modeling across morphological classes. The main observational and physical properties of the selected sources are summarized in Table 2.1, and a detailed description of each object is presented in the following subsections.

Property	**IC 1531**	**NGC 315**	**PKS 2153-69**
Position and distance			
Right Ascension (J2000)	$00^{\mathrm{h}}\,09^{\mathrm{m}}\,35.5^{\mathrm{s}}$	$00^{\mathrm{h}}\,57^{\mathrm{m}}\,48.9^{\mathrm{s}}$	$21^{\mathrm{h}}\,57^{\mathrm{m}}\,05.9^{\mathrm{s}}$
Declination (J2000)	$-32^{\circ}\,16'\,38''$	$+30^{\circ}\,21'\,09''$	$-69^{\circ}\,41'\,24''$
Redshift z	0.0256	0.0165	0.0283
Luminosity distance [Mpc]	~ 110	~ 71	~ 122
Host galaxy and classification			
Host galaxy type	E/S0	Giant elliptical	Elliptical
Morphological class	FR I	FR I	FR II
Excitation class	LERG	LERG	HERG
Fermi-LAT detection	4FGL	4FGL	Marginal

Table 2.1: Summary of the main observational and physical properties of the selected sources. Coordinates and redshifts were taken from the NASA/IPAC Extragalactic Database (NED) and from [24]. Luminosity distances were estimated from the redshift assuming a flat ΛCDM cosmology with $H_0 = 70$ km s^{-1} Mpc^{-1}.

2.1.1 IC 1531

IC 1531 is a nearby radio galaxy located at a redshift of $z \approx 0.0256$. The designation "IC" refers to the *Index Catalogue* [36, 37], an extension of the New General Catalogue compiled in the late 19th and early 20th centuries to include faint nebulae and galaxies that were missed in earlier surveys. The source is hosted by an early-type galaxy in the southern sky and has been observed across a broad range of wavelengths, from radio frequencies up to γ-ray energies.

Within the Fanaroff-Riley scheme, IC 1531 is classified as a low-power radio galaxy with morphological properties consistent with FR I sources and an optical spectrum compatible with a low-excitation radio galaxy (LERG). Its relativistic jet is interpreted as misaligned with respect to the line of sight, with viewing angles typically estimated in the range 10° to 20° [19]. High-resolution radio observations reveal a compact core-jet structure on parsec scales, and multiwavelength data confirm the non-thermal nature of the nuclear emission.

Figure 2.1 presents the large-scale radio morphology and the X-ray emission of IC 1531. The left panel shows the NVSS 1.4 GHz radio contours, revealing an extended structure of $\sim$220 kpc with two lobes characteristic of a radio galaxy. The right panel displays a Chandra X-ray image (0.5–7 keV) with superimposed VLA 8.5 GHz contours. The unresolved X-ray core coincides with the radio nucleus, while extended X-ray emission is visible along the jet direction and around the radio lobes, tracing the hot intracluster medium displaced by the relativistic outflow. This multiwavelength view highlights the complex interplay between the jet and the surrounding environment.

The source is included in the *Fermi*-LAT fourth source catalog (4FGL), with a significant detection at high-energy γ-rays [29], which makes IC 1531 one of the few misaligned AGNs firmly established as a γ-ray emitter. SSC modeling of its broadband emission has been previously performed by [19], who explored different viewing-angle configurations to reproduce the observed SED, and these models are used in the present work as a reference for comparison with our results.

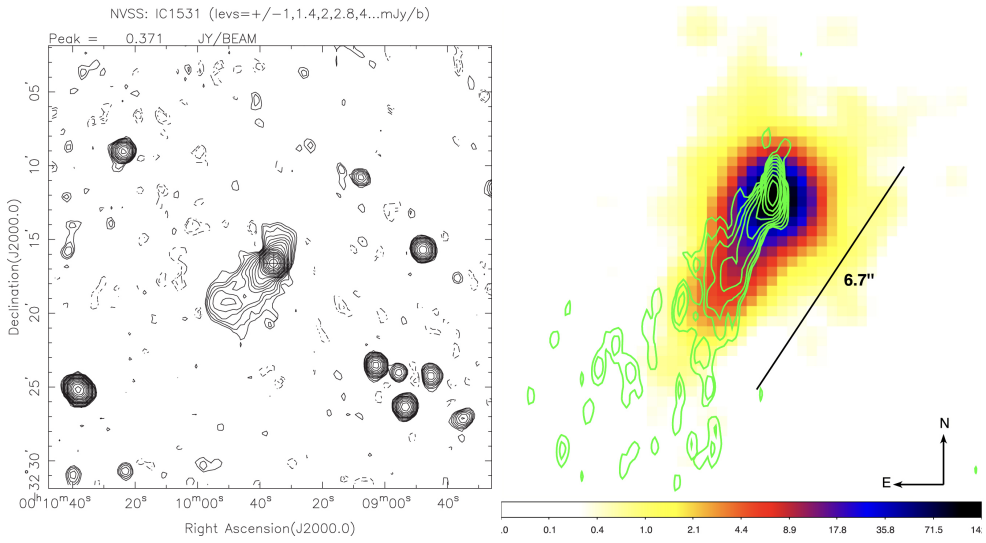

Figure 2.1: Radio and X-ray observations of the radio galaxy IC 1531. *Left:* NVSS 1.4 GHz contours showing the ∼220 kpc large-scale radio structure. *Right:* Chandra X-ray image (0.5–7 keV) with superimposed VLA 8.5 GHz radio contours, revealing the core-jet morphology and an extended X-ray halo. Adapted from [38].

2.1.2 NGC 315

NGC 315 is a nearby AGN located at a redshift of $z \approx 0.0165$, hosted by a giant elliptical galaxy in the constellation Pisces. The designation "NGC" refers to the *New General Catalogue* [39], one of the most widely used catalogs of deep-sky objects, compiled in the late 19th century. NGC 315 is one of the brightest and most extended FR I radio galaxies in the local Universe, and its large angular size has made it a benchmark source for the study of low-power relativistic jets.

The radio structure of NGC 315 extends over hundreds of kiloparsecs, with a well-resolved double-sided jet morphology that has been mapped at multiple frequencies. Figure 2.2 illustrates this multi-scale structure through a composite radio image. The left panel, obtained with the Westerbork Synthesis Radio Telescope (WSRT), shows the large-scale lobes at arcsecond resolution. The middle panel, from the Very Large Array (VLA), resolves the inner jet and counter-jet with greater detail. The right panel presents a Very Long Baseline Interferometry (VLBI) image at milliarcsecond resolution, revealing the compact core and the base of the relativistic jet. Together, these panels highlight the continuous collimated jet from parsec to kiloparsec scales.

Multifrequency radio observations show detailed spectral and morphological features along

the jet, suggesting spatial variations in particle acceleration and energy transport processes [26]. High-resolution X-ray observations performed with the *Chandra* X-ray Observatory have detected diffuse synchrotron emission from the inner regions of the jet, indicating the presence of high-energy electrons accelerated along the flow [26]. Recent ultraviolet observations have also revealed emission knots in the giant jet structure, suggesting localized regions of star formation or shock-induced emission [27].

NGC 315 hosts a low-luminosity AGN (LLAGN) powered by a SMBH with an estimated mass of the order of 10^8–$10^9\,M_\odot$. The broadband emission of the source extends from radio wavelengths to high-energy X-rays and γ-rays. The source is firmly detected by Fermi-LAT in the 4FGL catalog [29], and its broadband SED has been previously modeled in a leptonic framework by [18], providing the reference model adopted for comparison in Section 2.5.

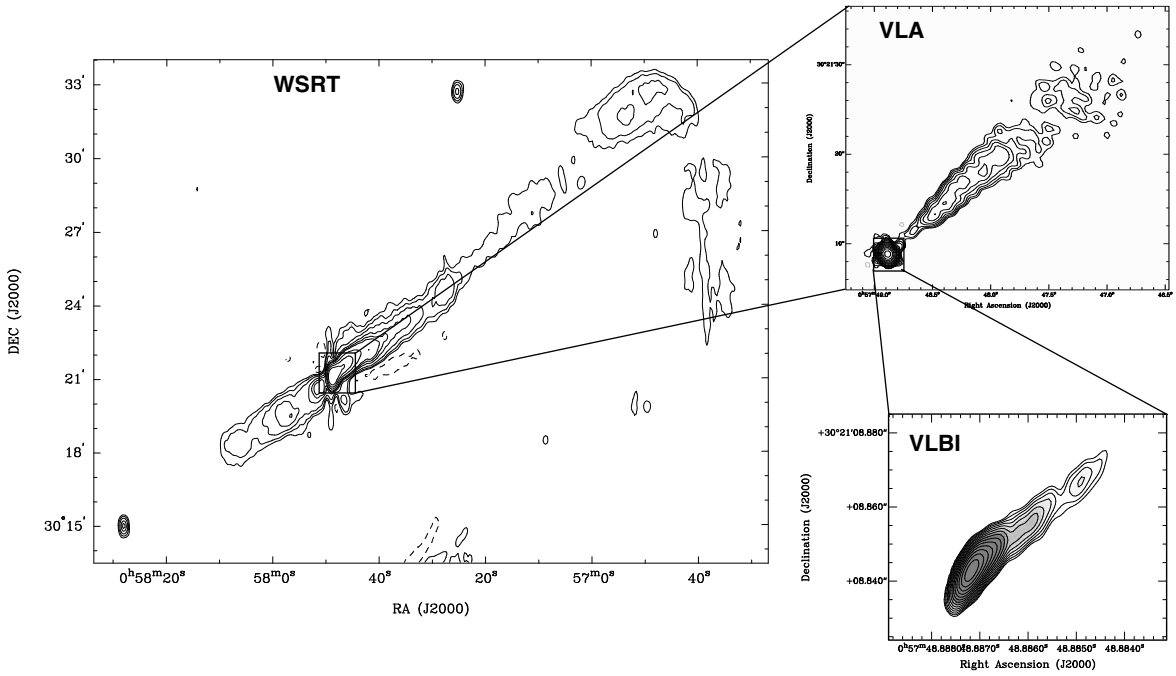

Figure 2.2: Radio continuum image of the radio galaxy NGC 315 at different angular resolutions: WSRT (left), VLA (middle), and VLBI (right). The contours and greyscale represent the radio emission from the core and jet, illustrating the structure from arcsecond to milliarcsecond scales. Contour levels of the WSRT image are -1, 1, 2, 4, 8, 12, 16, 32, 64, and 128 mJy beam^{-1}. Adapted from [40].

2.1.3 PKS 2153-69

PKS 2153-69 is a nearby radio galaxy hosting an active galactic nucleus with prominent jet activity, located at a redshift of $z \approx 0.0283$. The designation "PKS" refers to the *Parkes Catalogue of Radio Sources* [41], compiled from radio observations performed with the 64-m Parkes radio telescope in Australia. The source is hosted by a southern elliptical galaxy and represents one of the closest examples of an FR II radio galaxy, characterized by powerful relativistic jets that terminate in bright radio lobes and hot spots as they interact with the surrounding intergalactic medium.

Figure 2.3 presents the large-scale X-ray and radio morphology of PKS 2153-69. The Chandra X-ray image (0.5–7 keV) reveals a diffuse, roughly spherical halo of hot gas extending out to approximately 30 kpc. Overlaid as contours is an ATCA 4.7 GHz radio map, showing two prominent lobes on opposite sides of the nucleus. The southern lobe contains a bright hot spot, while the northern lobe appears more diffuse. Depressions in the X-ray surface brightness coincide with the radio lobes, indicating cavities that the relativistic jet has inflated in the hot intergalactic medium.

The radio morphology of PKS 2153-69 exhibits clear evidence of jet-environment interactions on kiloparsec scales, including pronounced hot spots, extended diffuse lobes, and regions where the jet interacts with surrounding gas clouds [25]. High-resolution radio observations reveal a one-sided parsec-scale jet emerging from the nucleus, consistent with relativistic outflows produced by accretion onto a central SMBH. Optical imaging performed with the Hubble Space Telescope has identified an emission-line knot located along the jet path, interpreted as the result of the interaction between the jet and a dense gas cloud in the inner host galaxy environment [25].

Very Long Baseline Interferometry (VLBI) observations from the TANAMI program have been used to study the parsec-scale structure and kinematics of the jet. These observations show that the jet extends tens of milliarcseconds from the core and exhibits apparent superluminal motion up to $\beta_{\rm app} \approx 3.6$, suggesting ongoing jet acceleration on scales of tens of parsecs [25]. Despite its prominent jet activity, PKS 2153-69 has not been firmly established as a strong γ-ray emitter by the Fermi-LAT, with only marginal detections reported in the 4FGL catalog [29]. This makes the source an especially interesting target for the next-generation CTAO detectability analysis discussed in Chapter 3.

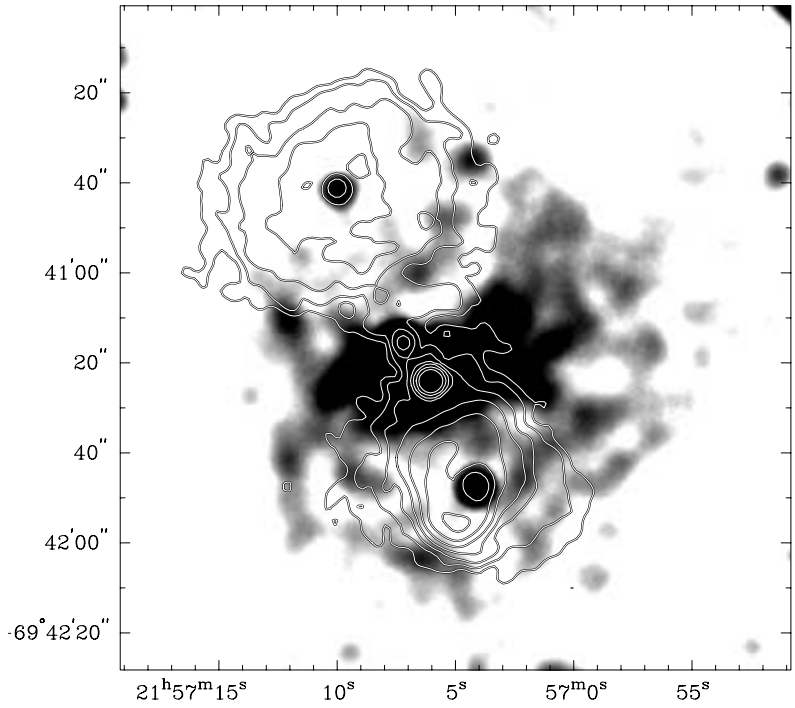

Figure 2.3: Chandra X-ray image (0.5–7 keV band) of the radio galaxy PKS 2153-69, overlaid with contours of an ATCA 4.7 GHz radio map [42]. The X-ray image reveals a diffuse, roughly spherical halo of hot gas extending out to ∼30 kpc. Depressions coincident with the radio lobes indicate cavities inflated by the jet. Adapted from [25].

2.2 Modeling Framework

A one-zone model is a simplified theoretical framework in which the broadband emission of an astrophysical source is assumed to originate from a single, homogeneous region within the relativistic jet. This emitting zone is characterized by uniform physical conditions, including the magnetic field strength, the particle energy distribution, and the bulk motion of the plasma. Within this region, radiative processes such as synchrotron emission and IC scattering are computed self-consistently, allowing the reproduction of the observed SED. Although this approach neglects the possible spatial complexity and stratification of the jet, it provides a robust and widely used approximation for modeling the main features of the non-thermal emission in AGNs, particularly when the data are too sparse to constrain more complex multi-zone scenarios [9, 8].

2.2.1 JetSeT Overview

To construct the SED of each source, we use the *JetSeT* framework [11, 12, 13]. JetSeT is an open-source Python package designed for the modeling and fitting of the broadband emission of relativistic jets. The package is built upon widely used scientific libraries such as Astropy [43] and SciPy [44], and provides optimization and parameter-estimation tools including Minuit minimization and Markov Chain Monte Carlo (MCMC) sampling through the `emcee` framework [45].

In this work, *JetSeT* is employed within a one-zone leptonic scenario to model the emission of the selected AGNs. The framework provides tools for handling and organizing multiwavelength observational data, including operations such as data selection, rebinning, and integration with astrophysical libraries such as *astropy*. The modeling procedure involves fitting theoretical models to the observed SEDs to constrain the physical parameters of the source. In particular, quantities such as the magnetic field strength, the bulk Lorentz factor, the viewing angle, and the particle energy distribution are derived through an iterative fitting process. The analysis begins with a pre-fitting stage, in which initial parameter values are estimated from phenomenological properties of the observed SED, such as spectral slopes, peak frequencies, and flux levels. These initial conditions are then refined through numerical optimization techniques, including Minuit-based algorithms and *scipy* least-squares methods, as well as Bayesian Markov Chain Monte Carlo (MCMC) approaches, leading to a consistent representation of the observed emission.

2.2.2 Radiative Processes

The modeling of SEDs of AGNs is primarily based on non-thermal radiative processes occurring in relativistic jets. In the framework adopted in this work, the emission is described within a leptonic scenario, where relativistic electrons are responsible for the observed radiation through synchrotron emission and IC scattering. The latter can occur either via SSC, where the seed photons are produced within the jet, or via external Compton (EC), where the seed photons originate from external radiation fields such as the accretion disk, the broad-line region, or the dusty torus.

Synchrotron. The synchrotron mechanism arises from relativistic electrons spiraling around magnetic field lines within the jet. As a result of their acceleration, these particles emit broadband radiation that typically extends from radio frequencies up to optical or X-ray energies. The characteristic frequency of synchrotron emission depends on both the electron energy and the magnetic field strength, making this process particularly important for constraining key physical parameters such as the magnetic field B and the electron energy distribution.

Synchrotron self-Compton (SSC). At higher energies, IC scattering becomes the dominant emission process. Relativistic electrons transfer part of their energy to low-energy photons, boosting them to X-ray and γ-ray energies. When the seed photons originate from the synchrotron radiation produced within the jet itself, the process is referred to as SSC. This mechanism is intrinsically linked to the synchrotron component and provides a self-consistent description of the broadband emission within a one-zone leptonic framework.

External Compton (EC). Alternatively, if the seed photons are external to the jet, such as those originating from the accretion disk, the broad-line region, or the dusty torus, the process is known as EC. This contribution can become significant in sources where external radiation fields are intense, particularly in luminous AGNs such as flat-spectrum radio quasars. Since the three sources analyzed in this work are low-luminosity radio galaxies with weak external photon fields, the EC contribution is expected to be subdominant, and the modeling is therefore restricted to the synchrotron and SSC processes.

The interplay between synchrotron, SSC, and EC processes leads to the characteristic double-peaked structure observed in the SEDs of many AGNs. The low-energy peak is associated with synchrotron emission, while the high-energy peak is generally attributed to IC processes [9, 8].

2.3 Methodology

The modeling of the SEDs of the selected active galactic nuclei was carried out through a multi-step procedure combining observational data analysis and numerical modeling. The methodology adopted in this work is based on a leptonic one-zone scenario and is implemented using the *JetSeT* framework.

In the first stage, multiwavelength observational data were collected for each source and organized to construct their SEDs. These datasets cover a broad range of frequencies, allowing the identification of the main emission components associated with the jet. The modeling process begins with the definition of an emission region characterized by a set of physical parameters, namely the magnetic field strength, the bulk Lorentz factor, the viewing angle, the size of the emitting region, and the parameters of the electron energy distribution. These parameters provide the initial conditions for the numerical modeling.

To obtain a first approximation of the SED, a phenomenological approach was employed. The low- and high-energy components of the spectrum were approximated using polynomial functions, allowing the identification of key features such as peak frequencies and fluxes. These quantities serve as input for the pre-fitting stage, providing reasonable initial estimates for the physical parameters of the model. Following this initial step, a numerical fitting procedure was performed using optimization algorithms implemented in *JetSeT*. In particular, the Minuit minimization method was used to refine the model parameters and achieve a better agreement between the theoretical SED and the observational data. In some cases, additional refinement of the parameter space was achieved through Bayesian methods, such as Markov Chain Monte Carlo (MCMC) sampling, which provides information about parameter uncertainties and correlations.

2.3.1 Pre-fitting Procedure

The modeling process begins with a pre-fitting stage aimed at obtaining a first approximation of the SED and providing physically motivated initial values for the model parameters. This step is essential to ensure the convergence and stability of the subsequent numerical fitting procedures. In this work, the pre-fitting stage is based on a phenomenological analysis of the SED. The low-energy and high-energy components of the spectrum, typically associated with synchrotron and IC emission, respectively, are approximated using polynomial functions. In particular, a third-degree polynomial is used to reproduce the general shape of each component in logarithmic space.

This approach allows the identification of key spectral features, such as the peak frequencies and peak fluxes of both components. These quantities are directly related to the physical properties of the emitting region, including the characteristic energies of the particle distribution and the magnetic field strength. The parameters obtained from this phenomenological description are

then used as initial guesses for the physical model implemented in *JetSeT*. This step significantly reduces the parameter space to be explored during the numerical fitting stage and improves the efficiency of the optimization process.

2.3.2 Parameter Estimation

After the pre-fitting stage, the model parameters are refined through numerical optimization techniques in order to achieve a quantitative agreement between the theoretical model and the observational data. In this work, the fitting procedure is primarily performed using the Minuit minimization algorithm, which is based on the minimization of a cost function, typically defined as a chi-square (χ^2) statistic. This method iteratively adjusts the model parameters to minimize the difference between the observed data points and the model predictions, providing an optimal set of parameters that best reproduces the SED.

The fitting process involves several iterations, during which the parameters are progressively refined. The initial values provided by the pre-fitting stage play a crucial role in guiding the optimization toward physically meaningful solutions and avoiding convergence to local minima. In addition to the standard statistical method implemented through Minuit, Bayesian methods such as MCMC sampling are employed to further explore the parameter space. These techniques allow the estimation of parameter uncertainties and correlations, providing a more complete statistical characterization of the model. The combination of both methods results in a robust determination of the physical parameters governing the emission processes, enabling a consistent interpretation of the observed SEDs.

After obtaining the best-fit solution with the Minuit minimization algorithm, an MCMC analysis was performed to explore the posterior probability distributions of the model parameters and to evaluate possible parameter degeneracies. The resulting corner plots are presented in Appendix A. In all three sources, the median values obtained from the MCMC chains are consistent with the Minuit best-fit solutions within the corresponding uncertainties, indicating that the optimization converged toward stable regions of the parameter space. The corner plots reveal moderate correlations among some parameters, particularly those related to the electron energy distribution and the physical properties of the emitting region. Nevertheless, the posterior distributions remain sufficiently constrained, supporting the robustness of the derived physical parameters.

2.3.3 Physical Diagnostics and Derived Quantities

In order to provide a physically meaningful interpretation of the modeled SEDs, a set of derived quantities is evaluated for each source. These quantities allow us to characterize the energy content of the emitting region, assess the relative importance of particles and magnetic fields, and constrain the dominant radiation mechanisms. Such diagnostics are commonly employed in leptonic and lepto-hadronic modeling to connect spectral fits with the underlying physical conditions in relativistic jets.

Electron Energy Distribution. The relativistic electron population responsible for the observed emission is commonly described by a broken power-law distribution [30], written as

$$N_e(\gamma_e) = N_{0,e} \begin{cases} \gamma_e^{-\alpha}, & \gamma_{\rm min} < \gamma_e < \gamma_{\rm b} \\ \gamma_{\rm b}^{\alpha_1-\alpha}\,\gamma_e^{-\alpha_1}, & \gamma_{\rm b} \leq \gamma_e < \gamma_{\rm max} \end{cases} \tag{2.1}$$

where $N_{0,e}$ is the normalization constant, α and α_1 are the spectral indices below and above the break, respectively, and $\gamma_{\rm min}$, $\gamma_{\rm b}$, and $\gamma_{\rm max}$ represent the minimum, break, and maximum Lorentz factors of the electron population. This parametrization is widely used in SED modeling of relativistic jets, as it provides a simple yet effective description of particle acceleration and cooling processes, where the break energy is often associated with a transition between acceleration-dominated and cooling-dominated regimes [20].

Magnetic Energy Density. The magnetic energy density is defined as

$$U_B = \frac{B^2}{8\pi}, \tag{2.2}$$

where B is the magnetic field strength. This quantity represents the energy stored in the magnetic field per unit volume and plays a key role in determining the efficiency of synchrotron radiation processes.

Electron Energy Density. The energy density of the relativistic electron population can be approximated as

$$U_e \approx n_e \langle\gamma\rangle m_e c^2, \tag{2.3}$$

where n_e is the electron number density, $\langle\gamma\rangle$ is the average Lorentz factor of the electron distribution, m_e is the electron mass, and c is the speed of light. The ratio U_e/U_B provides a direct

measure of the equipartition condition between particles and magnetic field. Values $U_e \gg U_B$ indicate a particle-dominated regime, while $U_e \sim U_B$ corresponds to approximate equipartition.

Doppler Factor. The Doppler factor is defined as

$$\delta = \frac{1}{\Gamma(1 - \beta \cos\theta)}, \tag{2.4}$$

where Γ is the bulk Lorentz factor, $\beta = v/c$, and θ is the viewing angle. This parameter quantifies the effect of relativistic boosting on the observed emission and directly impacts both the observed luminosity and the inferred intrinsic energetics of the source. As emphasized by [20], strongly particle-dominated solutions ($U_e/U_B \gg 1$) may reflect either efficient particle acceleration or limitations of the adopted one-zone model.

2.4 Leptonic Modeling Results

This section presents the results of the SED modeling for the three sources, obtained with the *JetSeT* framework under a one-zone leptonic scenario. The multiwavelength data are fitted using synchrotron and SSC processes. The initial parameters adopted in the pre-fitting stage are summarized in a single comparative table, followed by the SED figures and the best-fit parameters for each source. The physical interpretation of the results is discussed at the end of the section.

2.4.1 Initial Parameters

The initial parameter values adopted for the pre-fitting procedure of the three sources are listed in Table 2.2. The redshift is not treated as a free parameter in the fit and is included as metadata associated with the observational dataset. Magnetic field, bulk Lorentz factor, and viewing angle (or Doppler factor) values were taken from previous works available in the literature [19, 24, 26, 25]. Doppler factors for NGC 315 and PKS 2153-69 were computed using Eq. (2.4).

Parameter	**IC 1531**	**NGC 315**	**PKS 2153-69**
	Source property		
Redshift z	2.60×10^{-2}	1.60×10^{-2}	2.83×10^{-2}
	Emission region		
Magnetic field B [G]	3.61×10^{-1}	4.00×10^{-2}	1.93×10^{-1}
	Jet geometry and kinematics		
Viewing angle θ [deg]	15.00	~ 2 (initial)	0.0
Bulk Lorentz factor Γ	4.00	18	5.1
Doppler factor δ	~ 3.7	32.21	10.1

Table 2.2: Initial parameter values adopted in the pre-fitting procedure for the three sources. Values for IC 1531 were taken from [19] and [24], while NGC 315 and PKS 2153-69 initial parameters were taken from [24] and complemented with viewing-angle estimates from [26] and [25], respectively. The Doppler factors are computed using Eq. (2.4).

2.4.2 SED Fitting Results

The SEDs of the three sources, obtained with the Minuit fitting procedure and complemented by MCMC sampling, are presented in Figures 2.4–2.6. In each figure, the dashed green line represents the synchrotron component, the dashed red line corresponds to the SSC component, and the purple continuous line shows the total emission obtained as the sum of both contributions. The observational data are shown as colored markers corresponding to different experiments and catalogs.

IC 1531. Figure 2.4 shows the SED of IC 1531 obtained with the Minuit (top panel) and MCMC (bottom panel) procedures. The model reproduces the overall shape of the broadband emission, with the synchrotron component dominating from radio to optical energies and the SSC component accounting for the high-energy emission detected by Fermi-LAT.

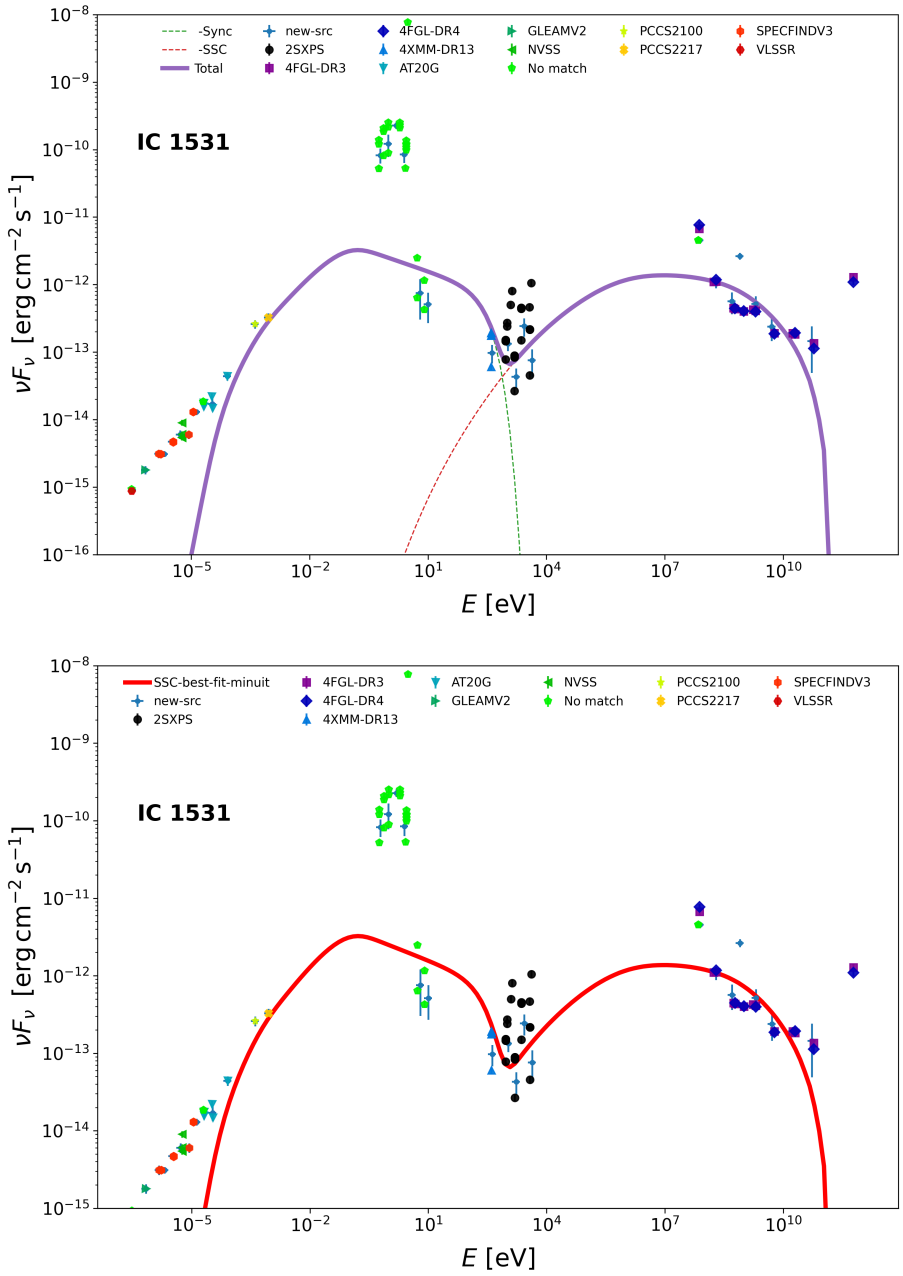

Figure 2.4: SED of IC 1531 modeled with a one-zone leptonic model using the Minuit fitting procedure (top) and the MCMC sampling (bottom). The dashed green line shows the synchrotron component, the dashed red line shows the SSC component, and the purple continuous line shows the total emission. The corresponding best-fit parameters are summarized in Table 2.3.

NGC 315. Figure 2.5 shows the SED of NGC 315 obtained with the Minuit (top panel) and MCMC (bottom panel) procedures. The model successfully reproduces the broadband emission from radio to γ-ray energies, although some dispersion remains in the optical-ultraviolet region,

where contributions from the host galaxy may also be present.

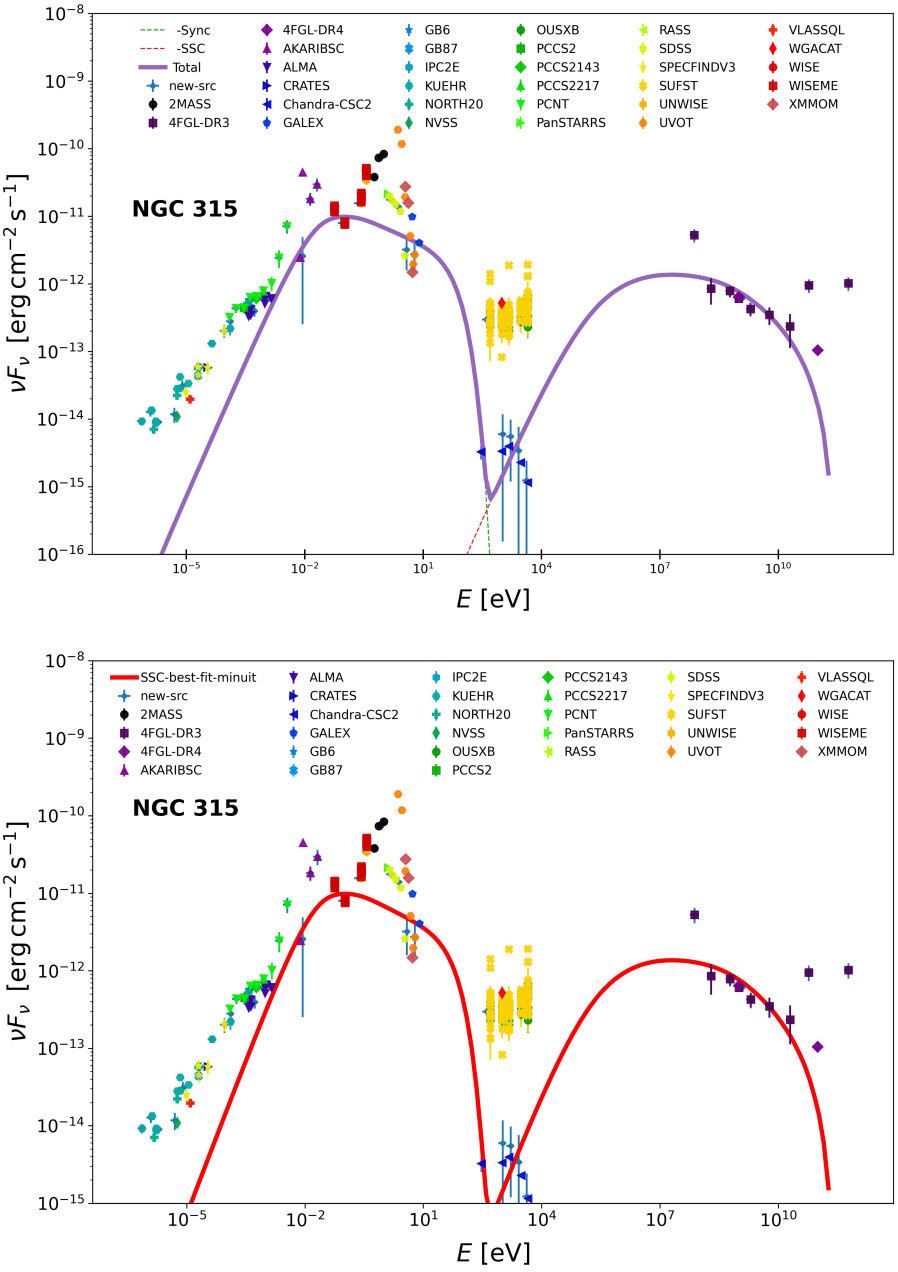

Figure 2.5: SED of NGC 315 modeled with a one-zone leptonic model using the Minuit fitting procedure (top) and the MCMC sampling (bottom). The line colors and styles are the same as in Figure 2.4. The corresponding best-fit parameters are summarized in Table 2.3.

PKS 2153-69. Figure 2.6 shows the SED of PKS 2153-69 obtained with the Minuit (top panel) and MCMC (bottom panel) procedures. The model captures the overall shape of the broadband emission, although the high-energy component is poorly constrained due to the limited

Fermi-LAT detection.

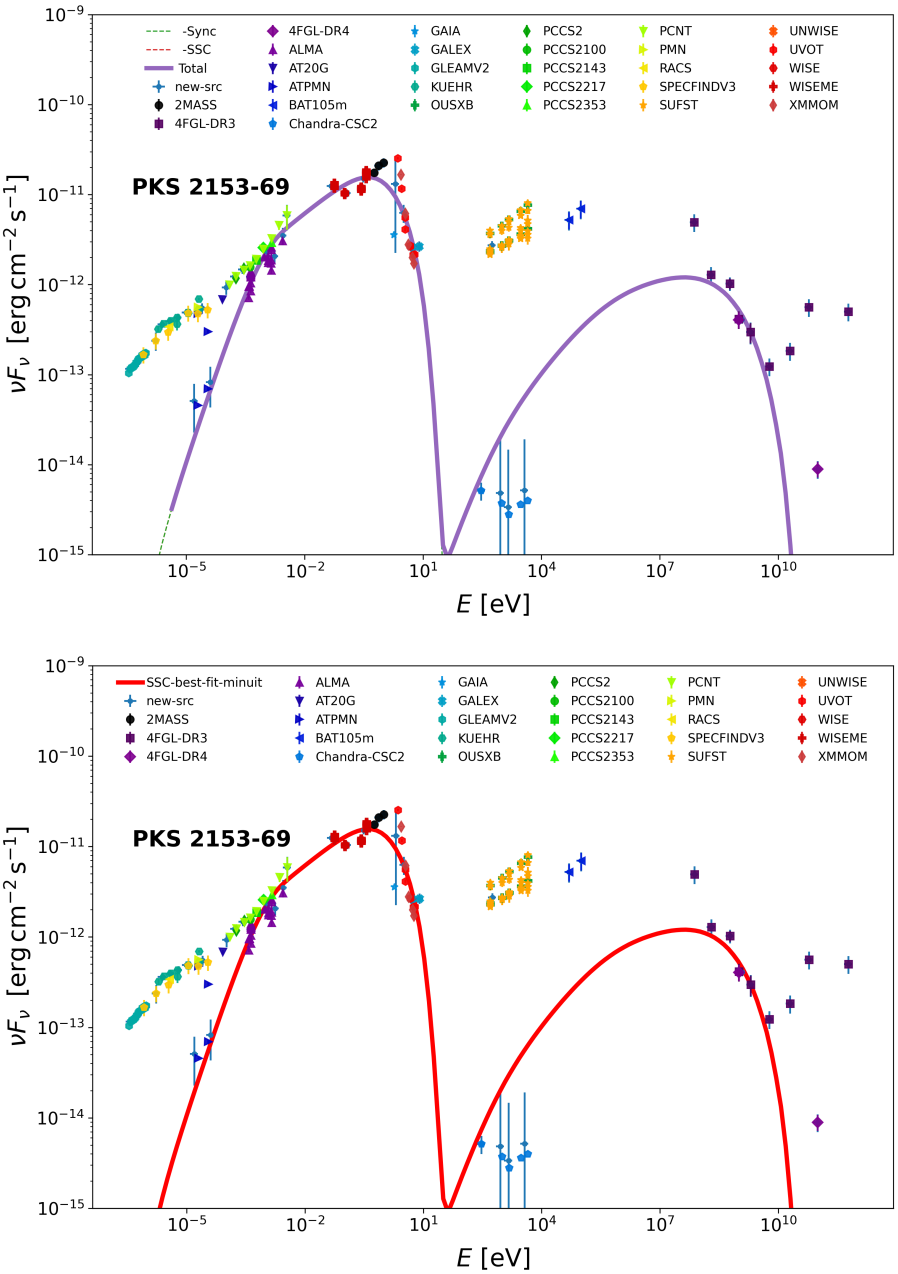

Figure 2.6: SED of PKS 2153-69 modeled with a one-zone leptonic model using the Minuit fitting procedure (top) and the MCMC sampling (bottom). The line colors and styles are the same as in Figure 2.4. The corresponding best-fit parameters are summarized in Table 2.3.

2.4.3 Best-Fit Parameters

The best-fit parameters obtained for the three sources after the Minuit minimization procedure are summarized in Table 2.3. The same set of parameters is presented for each source, allowing a direct comparison of the inferred physical conditions of the jets. Values marked with the dagger symbol (†) were kept fixed during the fitting process, either because they are intrinsic source properties (such as the redshift) or because they were adopted from previous studies (such as the geometrical configuration of IC 1531). Derived quantities such as the magnetic energy density, electron energy density, and Doppler factor are also reported.

Parameter	**IC 1531**	**NGC 315**	**PKS 2153-69**
	Source property		
Redshift $z^{\dagger}$	2.60×10^{-2}	1.60×10^{-2}	2.80×10^{-2}
	Emission region		
Magnetic field B [G]	$3.50 \times 10^{-1\,\dagger}$	$4.00 \times 10^{-2\,\dagger}$	3.23×10^{-2}
Radius R [cm]	$1.46 \times 10^{16\,\dagger}$	9.00×10^{16}	5.00×10^{17}
Emitter density n_e [cm^{-3}]	7.55×10^{1}	1.64×10^{-1}	4.91×10^{-2}
	Jet geometry and kinematics		
Viewing angle θ [deg]	$15^{\dagger}$	6.58	$10.0^{\dagger}$
Bulk Lorentz factor $\Gamma^{\dagger}$	$4^{\dagger}$	$18^{\dagger}$	$4.00^{\dagger}$
Doppler factor δ	~ 3.7	~ 7	~ 4.68
	Electron energy distribution		
$\gamma_{\rm min}$	1.32×10^{2}	1.73×10^{3}	5.02×10^{2}
$\gamma_{\rm b}$	2.09×10^{3}	5.51×10^{3}	1.35×10^{4}
$\gamma_{\rm max}$	1.00×10^{5}	1.00×10^{5}	3.29×10^{4}
Low-energy index α	1.66	2.67	2.28
High-energy index α_1	3.40	3.50	3.73
Spectral break $\Delta\alpha$	1.74	0.83	1.45
	Derived quantities		
U_B [erg cm^{-3}]	4.9×10^{-3}	6.4×10^{-5}	4.16×10^{-5}
U_e [erg cm^{-3}]	~ 0.13	$\sim 2.3 \times 10^{-4}$	$\sim 5.07 \times 10^{-5}$
U_e/U_B	~ 25	~ 3–4	~ 1.46

Table 2.3: Best-fit parameters obtained from the leptonic SED modeling of the three sources. Values marked with † were kept fixed during the fitting procedure. The spectral break is defined as $\Delta\alpha = \alpha_1 - \alpha$, and the derived quantities U_B, U_e, and δ are computed using Eqs. (2.2), (2.3), and (2.4), respectively.

2.4.4 Physical Interpretation

In this subsection, we discuss the physical implications of the SED modeling results for each source individually. The derived parameters are analyzed to characterize the emitting regions, assess the dominant radiation processes, and compare the properties of the three sources within the leptonic framework.

IC 1531. The SED of IC 1531 exhibits the characteristic double-peaked structure commonly observed in non-thermal jet sources. The low-energy component, extending from radio to optical frequencies, is well reproduced by synchrotron emission from a population of relativistic electrons. The position of the synchrotron peak ($\sim 10^{-2}$–1 eV) is consistent with a moderately energetic electron population characterized by a break Lorentz factor $\gamma_{\rm b} \approx 2.1 \times 10^3$. This relatively low break energy suggests that the dominant radiating electrons occupy a modest energy range. The high-energy component, extending up to $\sim 10^9$–10^{10} eV, is successfully reproduced through the SSC mechanism.

Using Eq. (2.2), the magnetic energy density is estimated as $U_B \approx 4.9 \times 10^{-3}\,\mathrm{erg\,cm^{-3}}$, while the electron energy density computed from Eq. (2.3) yields $U_e \approx 0.13\,\mathrm{erg\,cm^{-3}}$. The resulting ratio $U_e/U_B \sim 25$ indicates a strongly particle-dominated emission region, significantly out of equipartition. Such a condition may reflect efficient particle acceleration within the jet, although it can also point to intrinsic limitations of the one-zone modeling approach or parameter degeneracies. The bulk Lorentz factor ($\Gamma = 4$) and viewing angle ($\theta = 15^\circ$) imply a Doppler factor $\delta \sim 3.7$, corresponding to moderate relativistic boosting and supporting the interpretation of IC 1531 as a misaligned jet system rather than a strongly beamed blazar. The spectral steepening $\Delta\alpha = 1.74$ exceeds the canonical $\Delta\alpha = 1$ expected from standard synchrotron cooling, suggesting that the observed break reflects a combination of acceleration and cooling effects rather than radiative losses alone.

NGC 315. The SED of NGC 315 also displays a broadband structure that can be reasonably reproduced within a one-zone leptonic framework. The synchrotron peak is located around $E \sim 10^{-2}$–10^0 eV, indicating a dominant electron population with Lorentz factors $\gamma \sim 10^3$–10^4, consistent with the inferred break energy $\gamma_{\rm b} \approx 5.5 \times 10^3$. The high-energy component, extending up to $E \sim 10^7$–10^9 eV, is described by the SSC mechanism. The adopted magnetic field strength

$B = 0.04\,\mathrm{G}$, together with an emitting region size $R \approx 9\times10^{16}\,\mathrm{cm}$, points to a relatively extended emission region. The inferred particle density $n_e \approx 0.16\,\mathrm{cm}^{-3}$ is comparatively low, supporting a scenario in which the emission is produced in a dilute environment, consistent with the large-scale jet structures typically observed in FR I radio galaxies.

The resulting ratio $U_e/U_B \sim 3$–4 indicates a mildly particle-dominated emission region, close to equipartition. The bulk Lorentz factor $\Gamma = 18$ and viewing angle $\theta \approx 6.6°$ imply a Doppler factor $\delta \sim 7$, placing NGC 315 in an intermediate regime between classical radio galaxies and blazar-type sources. The spectral steepening $\Delta\alpha = 0.83$ is lower than the canonical value expected from standard synchrotron cooling, suggesting that the shape of the electron distribution may reflect a combination of acceleration processes and energy-dependent escape or transport effects within the emitting region. As discussed in Section 2.5, the relativistic configuration adopted in our fit differs substantially from the misaligned scenario considered by [18], leading to distinct physical interpretations.

PKS 2153-69. The SED of PKS 2153-69 also exhibits the characteristic double-peaked structure. The synchrotron peak is located around $E \sim 10^{-2}$–$10^{0}\,\mathrm{eV}$, indicating an electron population with Lorentz factors $\gamma \sim 10^3$–10^4, consistent with $\gamma_\mathrm{b} \approx 1.35 \times 10^4$. The high-energy component, extending into the γ-ray regime, is reproduced through SSC. The best-fit magnetic field $B \approx 0.03\,\mathrm{G}$ and emitting region size $R \sim 5 \times 10^{17}\,\mathrm{cm}$ describe a moderately magnetized and compact emission region. The particle density $n_e \sim 0.05\,\mathrm{cm}^{-3}$ and the resulting ratio $U_e/U_B \sim 1.46$ indicate a balanced energy distribution between particles and magnetic field. The bulk Lorentz factor $\Gamma \approx 4.0$ and viewing angle $\theta \approx 10°$ imply a Doppler factor $\delta \sim 4.68$, again consistent with moderate relativistic boosting.

The updated high-energy spectral index $\alpha_1 \approx 3.73$ and the resulting spectral break $\Delta\alpha \approx 1.45$ (with $\alpha \approx 2.28$) are significantly more physically plausible than preliminary iterations, aligning well with the canonical $\Delta\alpha \sim 1.0$ expected from standard synchrotron cooling. By allowing the emitting region radius to vary ($R \approx 5.0 \times 10^{17}$ cm), this fit resolves the artificial parameter boundary effects previously induced by the sparse high-energy constraints of the marginal Fermi-LAT detection. While minor discrepancies remain in the transition region between the synchrotron and SSC components, the updated one-zone leptonic model provides a physically consistent representation of PKS 2153-69's broadband SED without requiring extreme EED cutoffs.

It should be emphasized that several parameters exhibit degeneracy and are not tightly constrained by the available data, as indicated by the MCMC exploration. In particular, for NGC 315 and PKS 2153-69 the high-energy spectral indices reach the boundary of the explored parameter space, indicating that their values should be interpreted with caution. The derived physical quantities should therefore be regarded as representative of plausible solutions within the adopted one-zone framework rather than as unique physical descriptions.

2.5 Comparison with Previous Studies

In order to evaluate the consistency of the parameters obtained through our fitting procedure, we compare our results with values reported in previous studies available in the literature for each analyzed source. For IC 1531, we compare our results with the one-zone SSC modeling developed by [19], who explored different jet viewing-angle configurations for the source. For NGC 315, we use as a reference the SSC modeling presented by [18], who investigated the broadband emission of low-luminosity active galactic nuclei within the framework of leptonic jet models. For PKS 2153-69, no comparable SSC modeling is available in the recent literature, and the discussion of this source is therefore restricted to the present results.

In both cases where a literature comparison is possible, some of the parameters reported in the previous works were adopted as initial or fixed values during our fitting procedure, particularly those associated with the geometrical configuration and relativistic motion of the jet. Therefore, the comparison between our best-fit solutions and the published models allows us not only to verify the consistency of the obtained parameters but also to analyze how the free parameters evolved during the optimization process and how the resulting electron energy distributions compare with previous SSC descriptions of these sources.

2.5.1 IC 1531

The authors of [19] explored several SSC solutions for IC 1531 by varying the viewing angle θ. The corresponding models are summarized in Table 2.4.

θ [deg]	$\Gamma_{\rm bulk}$	$\gamma_{\rm min}$	$\gamma_{\rm max}$	$\gamma_{\rm b}$	$\log P_{\rm jet}$
5	10	180	5×10^6	8.0×10^3	44.38
12	4.5	180	5×10^6	9.0×10^3	44.04
15	4.0	180	5×10^6	9.0×10^3	43.69
20	2.0	180	5×10^6	7.5×10^3	43.33

Table 2.4: SSC model parameters for IC 1531 reported by [19] for different jet viewing angles. The jet power $P_{\rm jet}$ is given in erg s^{-1}.

For consistency with the SSC modeling of [19], the redshift, viewing angle, and bulk Lorentz factor were fixed during our fitting procedure using the values adopted in their $\theta = 15^\circ$ solution. The direct comparison between the best-fit parameters obtained in this work and those reported by [19] is shown in Table 2.5.

Parameter	**This work**	**De Rosa et al. [19]**
Source property		
Redshift z	2.60×10^{-2}	2.56×10^{-2}
Jet geometry and kinematics		
Viewing angle θ [deg]	15	15
Bulk Lorentz factor Γ	4	4
Electron energy distribution		
$\gamma_{\rm min}$	1.32×10^2	1.80×10^2
$\gamma_{\rm b}$	2.09×10^3	9.00×10^3
$\gamma_{\rm max}$	1.00×10^5	5.00×10^6
Low-energy index α	1.66	2.20
High-energy index α_1	3.40	3.40

Table 2.5: Comparison between the best-fit parameters obtained in this work for IC 1531 and the SSC model parameters reported by [19] for the case $\theta = 15°$.

As expected, the redshift, viewing angle, and bulk Lorentz factor coincide between the two analyses, since these parameters were fixed during our fitting procedure using the values adopted in the SSC modeling of [19]. The remaining parameters are generally consistent, although some differences are present. The minimum Lorentz factor of the electron population is of the same order of magnitude in both models, with our result yielding $\gamma_{\rm min} = 1.32 \times 10^2$ compared to $\gamma_{\rm min} = 1.80 \times 10^2$ in their work. The high-energy spectral index is practically identical, with $\alpha_1 = 3.40$ in our model and 3.4 in the solution by [19].

More significant differences are observed for $\gamma_{\rm max}$ and $\gamma_{\rm b}$. Our fit resulted in lower values for both parameters, namely $\gamma_{\rm max} = 1.00 \times 10^5$ and $\gamma_{\rm b} = 2.09 \times 10^3$, whereas [19] obtained $\gamma_{\rm max} = 5.00 \times 10^6$ and $\gamma_{\rm b} = 9.00 \times 10^3$. Despite these differences, the spectral indices remain relatively compatible, suggesting that the overall shape of the electron energy distribution is similar in both models. The low-energy spectral index obtained in this work, $\alpha = 1.66$, is reasonably close to the value $\alpha = 2.2$ adopted by [19], indicating comparable electron distributions in the low-energy

regime.

2.5.2 NGC 315

The comparison between the best-fit parameters obtained in this work for NGC 315 and the SSC model parameters reported by [18] is shown in Table 2.6.

Parameter	**This work**	**R. de Menezes et al. [18]**
	Source property	
Redshift z	1.60×10^{-2}	1.60×10^{-2}
	Emission region	
Magnetic field B [G]	4.00×10^{-2}	2.00×10^{-1}
Radius R [cm]	9.00×10^{16}	1.70×10^{16}
	Jet geometry and kinematics	
Viewing angle θ [deg]	6.58	38.00
Bulk Lorentz factor Γ	18.00	1.50
Doppler factor δ	~ 7	1.60
	Electron energy distribution	
$\gamma_{\rm min}$	1.73×10^{3}	1.00
$\gamma_{\rm b}$	5.51×10^{3}	2.00×10^{3}
$\gamma_{\rm max}$	1.00×10^{5}	2.70×10^{4}
Low-energy index α	2.67	2.00
High-energy index α_1	3.50	3.00

Table 2.6: Comparison between the best-fit parameters obtained in this work and the SSC model parameters reported by [18] for NGC 315.

The viewing angles obtained in this work and those adopted by [18] are substantially different,

indicating distinct physical interpretations for the jet orientation and relativistic beaming of NGC 315. In our modeling, the fit converged to a viewing angle of 6.58°, whereas [18] adopted a much larger angle of 38°. This discrepancy is directly related to the different relativistic parameters used in both works. Our fit was initially based on the values reported in [24], which provides a Doppler factor of $\delta = 32.21$. Such a high Doppler factor naturally implies a jet closely aligned with the line of sight, leading to a small viewing angle and strong relativistic boosting. Consistently, our fit also resulted in a large bulk Lorentz factor, $\Gamma = 18$, reinforcing the interpretation of a highly relativistic jet.

By contrast, [18] modeled NGC 315 as a misaligned FR I radio galaxy using much smaller relativistic parameters, namely $\delta = 1.6$ and $\Gamma = 1.5$. These values are compatible with a jet observed at a considerably larger angle, explaining the adopted viewing angle of 38°. The strong difference between the viewing angles, therefore, originates mainly from the distinct Doppler and bulk Lorentz factors adopted in each work. Our parameters describe a highly boosted and nearly aligned jet configuration, while the model of [18] assumes a mildly relativistic and significantly misaligned jet scenario for NGC 315. This dichotomy highlights the parameter degeneracies inherent to one-zone leptonic modeling, which can accommodate substantially different physical configurations while still providing acceptable fits to the broadband data.

2.6 Summary of the Chapter

In this chapter, the broadband SEDs of three nearby radio galaxies, namely IC 1531, NGC 315, and PKS 2153-69, were modeled within a one-zone leptonic framework using the *JetSeT* numerical package. A distinctive feature of the present analysis is the use of updated multiwavelength datasets compiled through the *Firmamento* platform [46], which combine recent catalog data and observations not available in earlier SED studies of these sources. The inclusion of these new data points provides improved spectral coverage across the radio, optical, X-ray, and γ-ray bands, allowing a more reliable characterization of the broadband emission compared to previous leptonic modeling of the same sources [19, 18]. The modeling included a phenomenological pre-fitting stage, a Minuit-based optimization, and an MCMC exploration of the parameter space. The main outcomes of the analysis can be summarized as follows.

The three sources display the characteristic double-peaked SED of non-thermal jet sources,

with the low-energy component well reproduced by synchrotron emission and the high-energy component accounted for by the SSC mechanism. The leptonic one-zone scenario therefore provides an acceptable description of the broadband emission of all three sources, despite their different morphological classes (FR I for IC 1531 and NGC 315, FR II for PKS 2153-69) and their different excitation regimes (LERG for IC 1531 and NGC 315, HERG for PKS 2153-69).

The break Lorentz factors γ_b span roughly one order of magnitude across the sample, ranging from $\sim 2.1 \times 10^3$ in IC 1531 and $\sim 5.5 \times 10^3$ in NGC 315 up to $\gamma_b \approx 1.35 \times 10^4$ in PKS 2153-69Ẇith the refined JetSeT fit, the inferred spectral breaks $\Delta\alpha = \alpha_1 - \alpha$ across all three sources now align closely with physical radiative expectations. In particular, PKS 2153-69 exhibits a spectral break of $\Delta\alpha \approx 1.45$ (with low-energy index $\alpha \approx 2.28$ and high-energy index $\alpha_1 \approx 3.73$), bringing it into strong agreement with the canonical $\Delta\alpha \sim 1.0$ expected from standard synchrotron radiative cooling losses [8]. Unfreezing the emitting region radius ($R \approx 5.0\times10^{17}$ cm) and adjusting the magnetic field ($B \approx 0.0323$ G) successfully relieved parameter degeneracies previously caused by the sparse high-energy Fermi-LAT photon statistics. This optimization resolved parameter boundary effects present in constrained fits, demonstrating that a single-zone leptonic SSC scenario provides a physically consistent description of PKS 2153-69's broadband SED without requiring unphysically steep electron energy distribution cutoffs.

The comparison with previous studies shows that the leptonic SED modeling of nearby radio galaxies suffers from significant parameter degeneracies, but also that the inclusion of new multiwavelength data leads to non-negligible refinements of the inferred physical parameters. In the case of IC 1531, our best-fit parameters are broadly consistent with those reported by [19] for the same viewing angle, with the largest differences appearing in $\gamma_{\rm max}$ and $\gamma_{\rm b}$, which are now better constrained by the additional high-energy data included in our analysis. In the case of NGC 315, our solution and that of [18] describe substantially different physical scenarios, namely a strongly boosted nearly aligned jet in our case and a mildly relativistic misaligned jet in theirs, while still providing acceptable fits to the broadband data. This dichotomy reinforces the well-known difficulty of constraining the Doppler factor simultaneously, the bulk Lorentz factor, and the viewing angle from SED modeling alone, and highlights the importance of complementary observational constraints, such as VLBI kinematics or independent estimates of the jet inclination.

From a methodological standpoint, the chapter also illustrates the practical limitations of one-zone leptonic modeling when applied to misaligned radio galaxies. For PKS 2153-69, the sparse high-energy coverage due to the marginal Fermi-LAT detection leads to a poorly constrained

high-energy index, while for NGC 315 the high-energy spectral index reaches the boundary of the explored parameter space. In both cases, the derived parameters should be interpreted as representative of plausible solutions within the adopted framework, rather than as unique physical descriptions of the sources.

Despite these limitations, the SED modeling carried out in this chapter provides an updated and consistent description of the broadband emission of the three selected sources, based on the most recent multiwavelength datasets available, and yields the spectral parameters used as input for the very-high-energy analysis presented in the next chapter. In particular, the high-energy components reproduced by the SSC mechanism are extrapolated to the energy range covered by the CTAO, allowing a quantitative assessment of the detectability of these misaligned AGNs with current and next-generation imaging atmospheric Cherenkov telescopes. The combination of updated multiwavelength SED modeling and CTAO detectability analysis, developed in Chapter 3, thus offers a self-consistent framework to investigate the role of nearby radio galaxies as candidate γ-ray and multi-messenger sources.

Chapter 3

Cherenkov Telescope Array (CTAO) Detectability Analysis

This chapter extends the analysis presented in Chapter 2 to the very-high-energy (VHE) regime, with the goal of evaluating the detectability of IC 1531, NGC 315, and PKS 2153-69 with the CTAO [17]. The HE spectral models obtained from the SED fitting are extrapolated to TeV energies, complemented by spectral fits to Fermi-LAT data, and folded with the instrumental response of CTAO. The analysis is carried out using the *Gammapy* library [28] together with the *FeuPy* framework, which provides tools for source association, visibility computation, observation simulation, and sensitivity evaluation.

The chapter is organized as follows. Section 3.1 describes the methodology adopted in this work, including the construction of HE models, the identification of γ-ray counterparts, the computation of source visibility, and the detectability criteria. Section 3.2 presents a comparative analysis of the three sources, addressing in turn the construction of the regions of interest (ROIs), the HE spectral fits, and the visibility from the CTAO arrays. Section 3.3 discusses the detectability of each source individually, addressing the specific observational and spectral features that affect its detection prospects. Finally, Section 3.4 provides a global discussion and summary of the chapter.

3.1 Very-high-energy (VHE) Methodology

The CTAO is designed to achieve unprecedented sensitivity in the energy range from a few tens of GeV up to several tens of TeV, enabling detailed studies of non-thermal emission from astrophysical sources [17]. In order to assess whether the predicted HE emission of the selected sources can be detected by CTAO under realistic observational conditions, we combine the spectral models derived in Chapter 2 with the instrumental response of the observatory. The methodology consists of four interconnected steps, namely HE spectral modeling, source association with existing catalogs, visibility computation for the CTAO arrays, and evaluation of the detection significance.

3.1.1 VHE Spectral Modeling with Gammapy

The VHE emission of the selected sources is modeled using the *Gammapy* package [28]. The spectral models obtained from the SED fitting with *JetSeT* are used as input and extrapolated to the VHE regime covered by CTAO. In this work, the differential photon flux is described using both a simple power-law (PL) model and a log-parabola (LP) model. The PL model is given by

$$\phi(E) = \phi_0 \left(\frac{E}{E_0} \right)^{-\alpha}, \tag{3.1}$$

where ϕ_0 is the differential flux normalization at the reference energy E_0, and α is the photon spectral index. The LP model is described by

$$\phi(E) = \phi_0 \left(\frac{E}{E_0} \right)^{-\alpha - \beta \log\left(\frac{E}{E_0}\right)}, \tag{3.2}$$

where β characterizes the spectral curvature. The corresponding SED, shown in the figures as νF_ν, is related to the differential photon flux through

$$\nu F_\nu(E) = E^2 \phi(E). \tag{3.3}$$

The PL model provides a simple description of non-thermal emission processes and is widely used to characterize HE and VHE gamma-ray spectra. The choice of this spectral representation is guided by the information available in the *Fermi*-LAT catalogs and by the quality of the spectral fit obtained for each source.

The expected number of detected photons is obtained by folding the spectral model with the CTAO instrumental response,

$$N_\gamma = \int_{E_{\min}}^{E_{\max}} \phi(E)\, A_{\text{eff}}(E)\, t_{\text{obs}}\, dE, \tag{3.4}$$

where $A_{\text{eff}}(E)$ is the effective area of the instrument and t_{obs} is the observation time.

In addition to the intrinsic spectrum, the propagation of VHE γ-rays through intergalactic space is affected by interactions with the Extragalactic Background Light (EBL), a diffuse radiation field composed primarily of ultraviolet, optical, and infrared photons accumulated throughout the history of the Universe. The dominant interaction is electron-positron pair production ($\gamma_{\text{VHE}} + \gamma_{\text{EBL}} \rightarrow e^+ + e^-$), which attenuates the observable γ-ray flux, particularly at energies above a few hundred GeV.

3.1.2 Source Association and Counterparts

The identification of γ-ray counterparts is performed by cross-referencing the positions of the selected sources with existing astronomical catalogs, ensuring that the modeled emission is consistent with previously detected high-energy sources. The *FeuPy* framework facilitates this process by integrating multiple catalogs and providing tools for positional matching. In particular, it allows the identification of counterparts in the Fermi-LAT third source catalog (3FGL) and fourth source catalog (4FGL) [29].

For each source, a circular region of interest (ROI) is defined around the nominal target position. The radius of the ROI is chosen as 0.5° for the counterpart search, while a smaller radius of 0.11° is used for the detailed visualization of the field around the source, which is appropriate given the angular resolution of CTAO and the positional uncertainties of the Fermi-LAT catalogs. The number of catalogued sources within the ROI, together with their angular separations from the target position, provides a measure of the complexity of the γ-ray environment and helps to assess whether the modeled emission can be unambiguously attributed to a single counterpart or whether contributions from neighboring sources need to be considered [21].

3.1.3 Visibility Computation

The visibility of each source is evaluated based on its sky coordinates and the geographical location of the CTAO observatories, which consist of two arrays located respectively at the Roque

de los Muchachos Observatory in La Palma (CTAO North) and at the European Southern Observatory in Paranal, Chile (CTAO South). The total observation time available for each source depends not only on its declination but also on observational constraints such as the zenith angle and the available exposure time. Observations performed at large zenith angles lead to a reduction in sensitivity due to atmospheric effects and an increase in the effective energy threshold. For this reason, the visibility is computed at three reference zenith angles (20°, 40°, 60°) for both arrays, and only observations within a suitable range of zenith angles are considered for the detectability assessment.

3.1.4 Detectability Criteria

The detectability of each source is evaluated using the standard ON/OFF observation method, widely adopted in imaging atmospheric Cherenkov telescopes. In this approach, the ON region contains both source and background events, while the OFF region is used to estimate the background contribution. The number of excess events attributed to the source is given by

$$N_S = N_{\mathrm{ON}} - \alpha\, N_{\mathrm{OFF}}, \tag{3.5}$$

where α is a normalization factor that accounts for differences in exposure and solid angle between the ON and OFF regions. The statistical significance of the detection is computed using the Li & Ma formula,

$$S = \sqrt{2}\left\{ N_{\mathrm{ON}} \ln\left[\frac{1+\alpha}{\alpha}\left(\frac{N_{\mathrm{ON}}}{N_{\mathrm{ON}}+N_{\mathrm{OFF}}}\right)\right] + N_{\mathrm{OFF}} \ln\left[(1+\alpha)\left(\frac{N_{\mathrm{OFF}}}{N_{\mathrm{ON}}+N_{\mathrm{OFF}}}\right)\right]\right\}^{1/2}. \tag{3.6}$$

A source is considered detectable if its significance exceeds the standard threshold of $S \geq 5\sigma$ and if the predicted flux lies above the CTAO sensitivity curve for the corresponding observation time. This framework provides a quantitative connection between the modeled HE emission and the observational capabilities of CTAO.

3.2 Comparative Analysis of the Three Sources

In this section, we present a comparative analysis of the three sources, addressing in sequence the construction of the regions of interest, the spectral modeling of the HE emission, and the

visibility from the CTAO arrays. This comparative approach allows a more direct identification of the similarities and differences between the sources before discussing each detectability case individually in Section 3.3.

3.2.1 Regions of Interest and Counterparts

The ROIs centered on the three sources were constructed following the procedure described in Section 3.1.2, with counterpart searches performed against the Fermi-LAT 3FGL and 4FGL catalogs. The maps of the ROIs are shown in Figure 3.1, and the identified counterparts with their angular separations from the nominal target positions are summarized in Table 3.1.

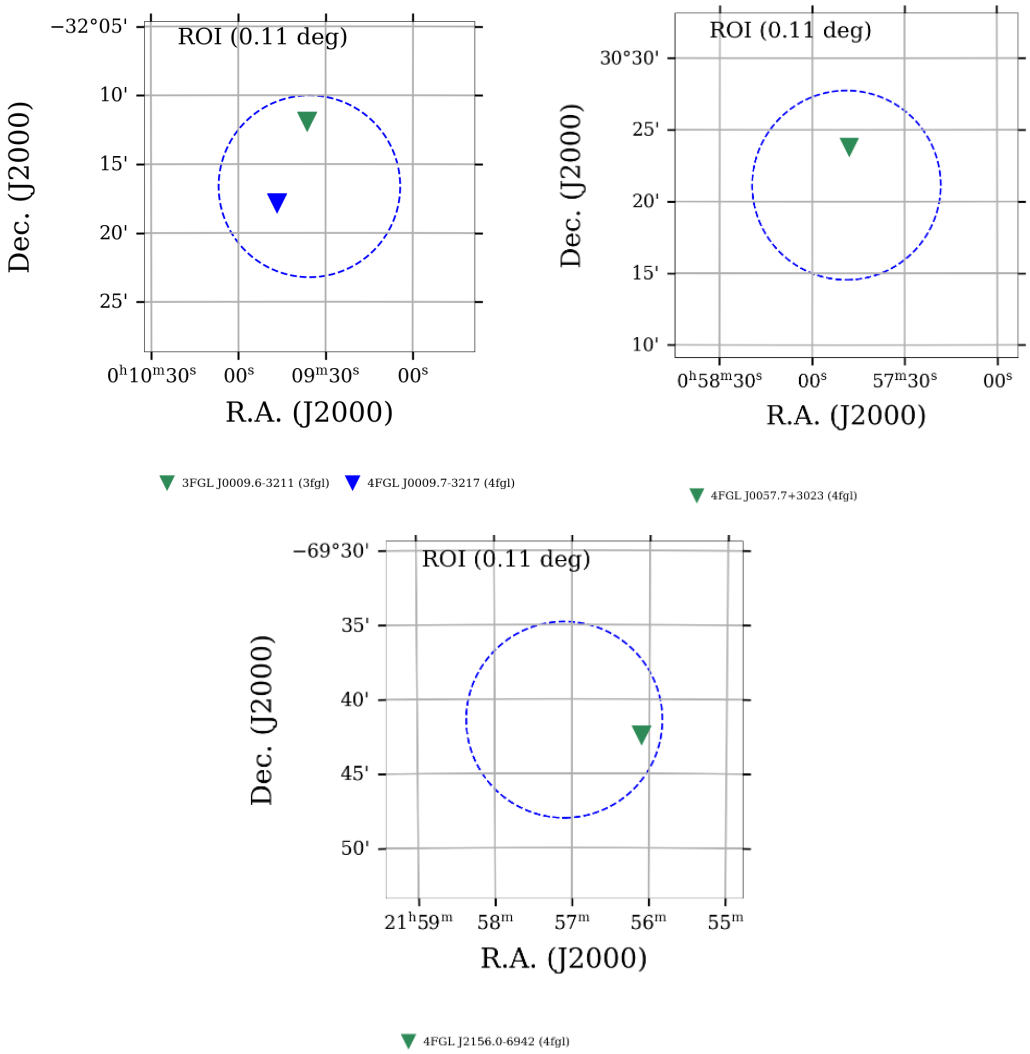

Figure 3.1: Regions of interest (radius 0.11°) centered on IC 1531 (top left), NGC 315 (top right), and PKS 2153-69 (bottom), in equatorial coordinates (J2000). The dashed blue circles represent the ROIs used in the analysis. Colored markers indicate γ-ray counterparts from the Fermi-LAT 3FGL and 4FGL catalogs.

Counterpart	R.A. [deg]	Dec. [deg]	Sep. [deg]
	IC 1531		
3FGL J0009.6-3211	2.402	−32.199	0.078
4FGL J0009.7-3217	2.444	−32.298	0.044
	NGC 315		
4FGL J0057.7+3023	14.450	+30.397	0.045
	PKS 2153-69		
4FGL J2156.0-6942	329.025	−69.707	0.088

Table 3.1: Counterparts identified within the ROI of each source from cross-matching with the Fermi-LAT 3FGL and 4FGL catalogs. Coordinates are given in the International Celestial Reference System (ICRS), and Sep. denotes the angular separation between the counterpart and the nominal target position.

The three sources display different levels of complexity in their γ-ray environments. IC 1531 is associated with two counterparts within the ROI, one from the 3FGL and one from the 4FGL catalog, with small angular separations from the target position (0.078° and 0.044°, respectively). The presence of two catalogued sources may indicate either a single physical source with an updated localization between catalog versions or a more complex region with contributions from multiple emitters. NGC 315 and PKS 2153-69, on the other hand, are associated with a single Fermi-LAT counterpart each (4FGL J0057.7+3023 and 4FGL J2156.0-6942, respectively), with small angular separations (0.045° and 0.088°), indicating relatively clean fields with minimal contamination from neighboring sources.

3.2.2 VHE Spectral Modeling

For each source, the Fermi-LAT spectrum was modeled using one of the parametrizations introduced in Section 3.1.1, namely a PL (Eq. 3.1) for IC 1531 and NGC 315 and a LP (Eq. 3.2) for PKS 2153-69. The choice of the LP model for PKS 2153-69 reflects the spectral curvature reported in the 4FGL catalog, while the PL model provides an adequate description of the data

for the other two sources within the analyzed energy range. The best-fit spectral parameters are summarized in Table 3.2.

Source	ϕ_0 **[TeV^{-1} cm^{-2} s^{-1}]**	E_0 **[TeV]**	α	β
		Power-law (PL)		
IC 1531	$(1.23 \pm 0.10) \times 10^{-9}$	0.010	2.34 ± 0.02	—
NGC 315	$(1.10 \pm 0.09) \times 10^{-9}$	0.010	2.36 ± 0.03	—
		Log-parabola (LP)		
PKS 2153-69	3.48×10^{-7}	0.001	2.36 ± 0.05	-0.16

Table 3.2: Best-fit parameters of the HE spectra of the three sources, obtained from Fermi-LAT data. The PL model is given by Eq. (3.1) and the LP model by Eq. (3.2). The amplitude ϕ_0 is given at the reference energy E_0.

The spectral indices of the three sources are remarkably similar, all clustered around $\alpha \approx 2.34$–2.36, consistent with typical values observed in AGN γ-ray spectra [20]. This similarity supports a common non-thermal origin of the HE emission, dominated by relativistic particles in the jets. The main qualitative difference is the presence of curvature in the spectrum of PKS 2153-69, with $\beta = -0.16$, indicating a deviation from a simple power-law behavior and suggesting either a more complex particle acceleration or cooling process, or an intrinsic high-energy cutoff in the emitting electron distribution.

The HE spectra of the three sources, including the extrapolation to the energy range covered by CTAO and the corresponding simulated flux points for a 50-hour observation, are shown in Figure 3.2.

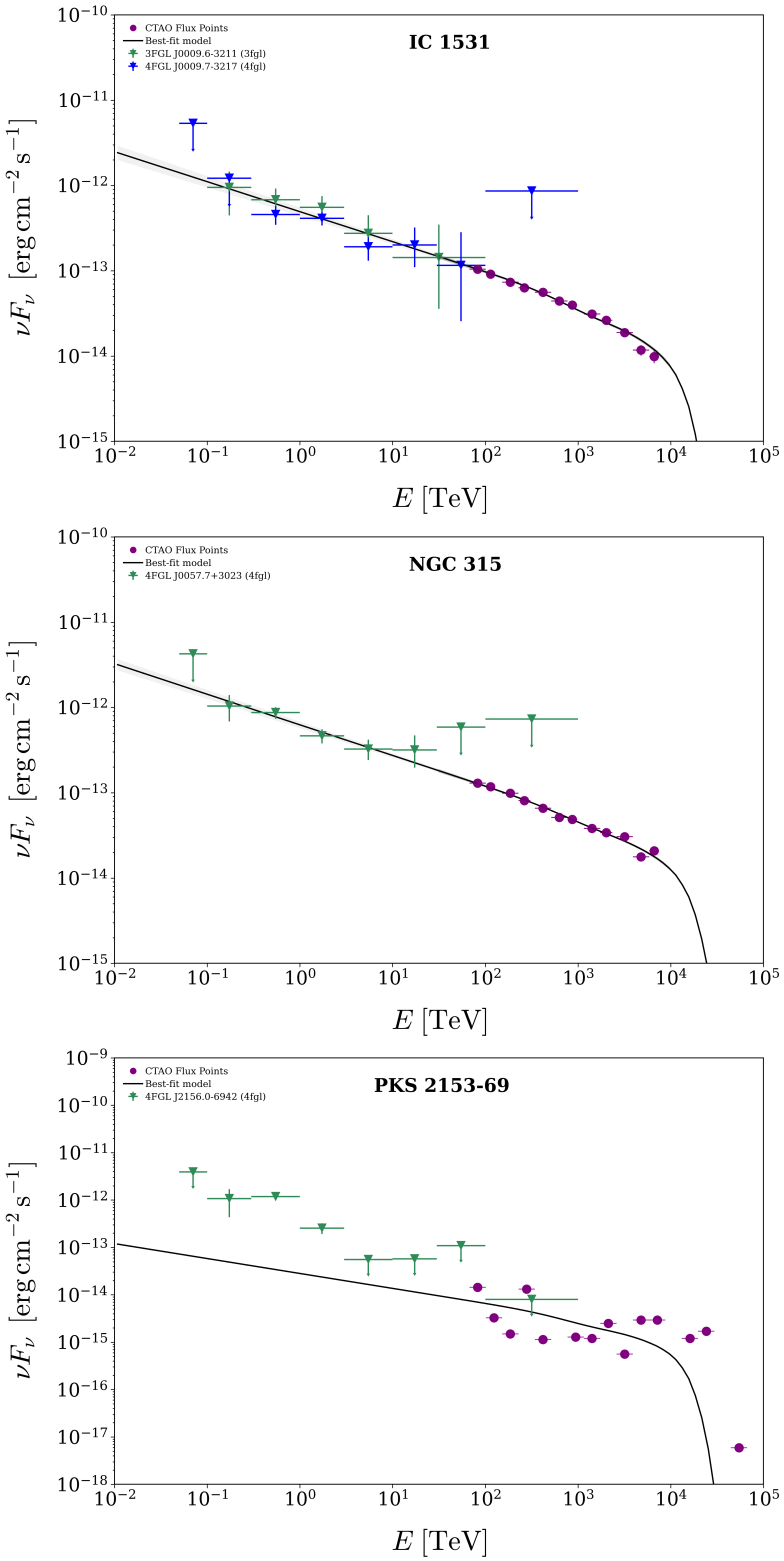

Figure 3.2: HE spectra of IC 1531 (top), NGC 315 (middle), and PKS 2153-69 (bottom). The black solid line represents the absorbed spectrum model, the colored markers correspond to observational data from the Fermi-LAT 3FGL and 4FGL catalogs, and the purple circles show the simulated flux points for a 50-hour CTAO observation and 100-hour for PKS 2153-69.

3.2.3 Visibility from the CTAO Arrays

The visibility of the three sources from the CTAO North and South arrays was computed at three reference zenith angles, namely 20°, 40°, and 60°. The results, expressed in cumulative observation hours per year above the corresponding zenith angle limit, are summarized in Table 3.3.

Zenith angle	**IC 1531 [h]**	**NGC 315 [h]**	**PKS 2153-69 [h]**
CTAO South (Paranal, Chile)			
20°	271.5	—	—
40°	241.0	—	419.0
60°	266.5	399.5	1670.5
CTAO North (La Palma, Spain)			
20°	—	381.0	—
40°	—	386.0	—
60°	682.0	394.0	—

Table 3.3: Visibility of the three sources from the CTAO North and South arrays at different zenith angles, expressed in cumulative observation hours per year above the corresponding zenith limit. Entries marked with "—" indicate that the source is not observable from the given array at the considered zenith angle.

The visibility analysis clearly illustrates the geographic complementarity between the two CTAO arrays. IC 1531 and PKS 2153-69, both located in the southern sky, are preferentially observable from CTAO South, with extended exposure times available across all zenith angles for IC 1531 and very large exposure times at moderate-to-high zenith angles for PKS 2153-69. NGC 315, on the other hand, is located in the northern sky and is therefore primarily observable from CTAO North, with stable exposure times across all zenith angles. This complementarity is one of the main strengths of the CTAO design, ensuring full-sky coverage of extragalactic γ-ray sources.

3.3 Source-by-source Detectability

In this section, the detectability of each source with CTAO is evaluated individually. For each source, the modeled HE flux is compared with the CTAO differential sensitivity curve corresponding to a 50-hour observation, and the simulated number of ON and OFF counts is used to compute the detection significance via the Li & Ma formula (Eq. 3.6). The discussion below addresses the specific spectral and environmental features that influence the detection prospects of each source.

3.3.1 IC 1531

The HE spectrum of IC 1531 is well described by a power law with spectral index $\alpha \approx 2.34$, consistent with a non-thermal origin dominated by relativistic particles in the jet. The presence of two catalogued counterparts within the ROI (3FGL J0009.6-3211 and 4FGL J0009.7-3217) introduces a moderate level of complexity in the γ-ray environment, as overlapping contributions from neighboring sources may affect the derived spectral parameters and the background estimation.

Figure 3.3 shows the comparison between the modeled spectrum, the EBL-absorbed spectrum, and the CTAO differential sensitivity curve for a 50-hour observation. The intrinsic flux lies above the sensitivity curve over a significant portion of the energy range below ~ 1 TeV, while the EBL-attenuated spectrum approaches the sensitivity limit at higher energies. This indicates that IC 1531 should be detectable by CTAO in the sub-TeV range, although the contribution of the EBL absorption becomes increasingly important above a few hundred GeV. The simulated ON/OFF analysis (Figure 3.4) yields a detection significance compatible with the 5σ threshold for the assumed exposure, supporting the classification of IC 1531 as a viable CTAO target.

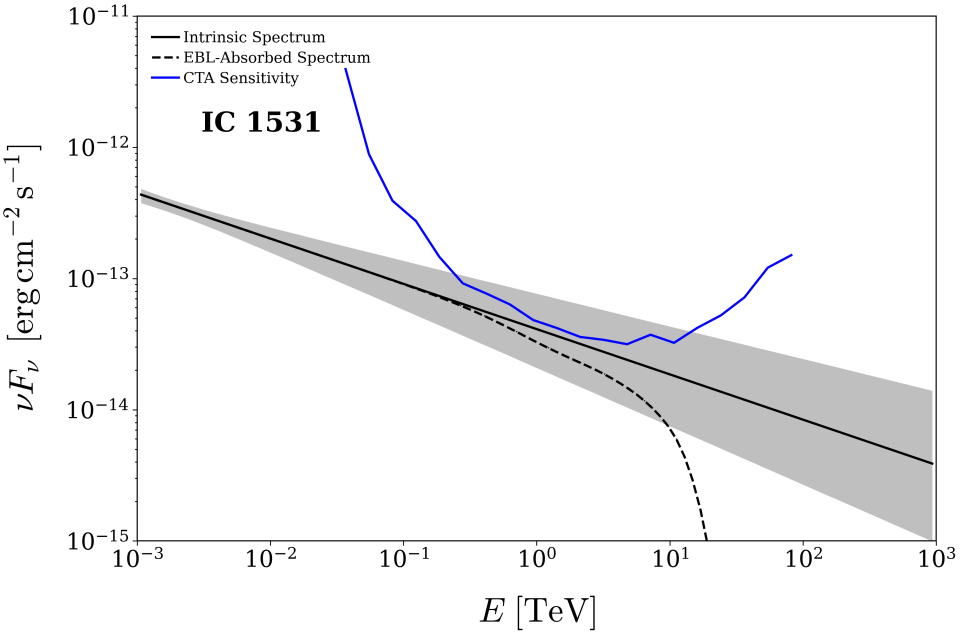

Figure 3.3: Energy-dependent differential flux sensitivity and model predictions for the IC 1531 region. The black solid line represents the intrinsic extrapolated spectrum, the dashed line represents the EBL-absorbed spectrum, and the blue line shows the CTAO sensitivity curve for a 50-hour observation.

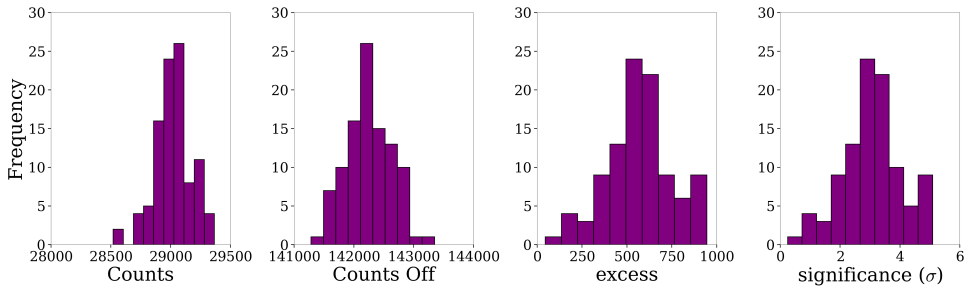

Figure 3.4: Distribution of simulated ON counts, OFF counts, excess counts, and detection significance (Eq. 3.6) for the IC 1531 region, obtained for 100 realizations of a 50-hour CTAO observation.

3.3.2 NGC 315

The HE spectrum of NGC 315 is also well described by a simple power law, with a spectral index $\alpha \approx 2.36$, indicating a non-thermal origin similar to that inferred for IC 1531. The ROI of NGC 315 contains a single Fermi-LAT counterpart (4FGL J0057.7+3023), positionally coincident

with the target source, which makes this the cleanest field among the three analyzed sources and reduces the systematic uncertainties associated with source confusion and background estimation.

The comparison between the modeled spectrum and the CTAO sensitivity is shown in Figure 3.5. The intrinsic flux lies marginally above the CTAO sensitivity curve in the sub-TeV range, with EBL absorption playing a non-negligible role above several hundred GeV. The simulated counts distribution (Figure 3.6) is consistent with a marginal detection at the 5σ level for a 50-hour exposure, suggesting that longer observation times or stacked observations may be required to achieve a robust detection. Despite the moderate flux level, the clean ROI and the strong visibility from CTAO North make NGC 315 an excellent target for future HE studies.

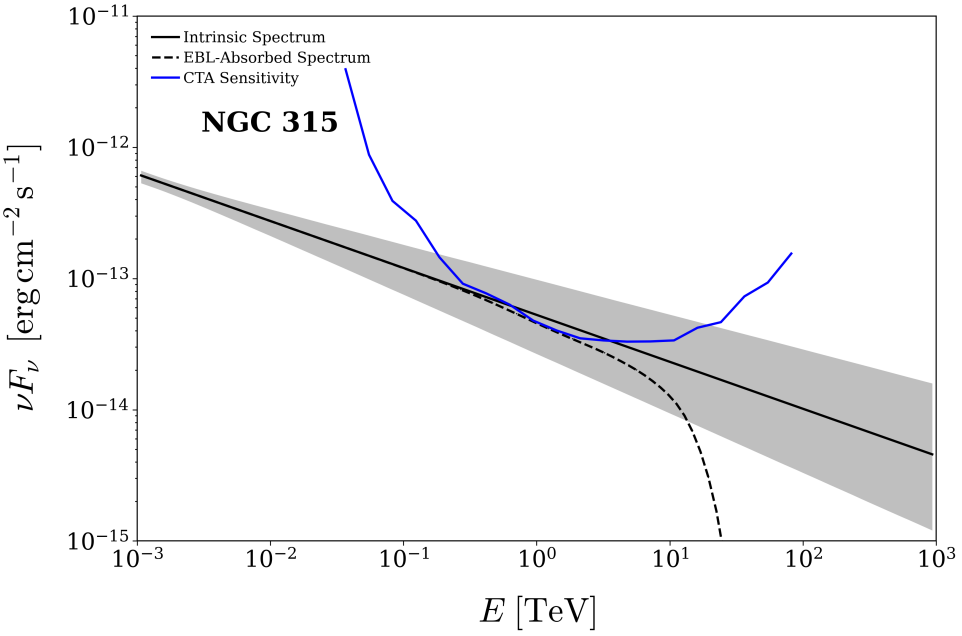

Figure 3.5: Energy-dependent differential flux sensitivity and model predictions for the NGC 315 region. The line styles are the same as in Figure 3.3.

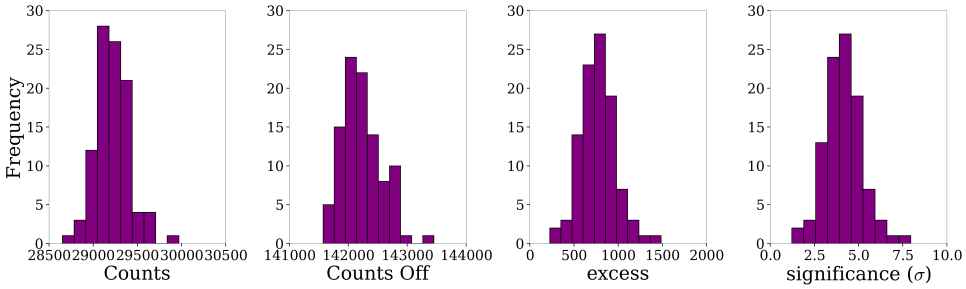

Figure 3.6: Distribution of simulated ON counts, OFF counts, excess counts, and detection significance (Eq. 3.6) for the NGC 315 region, obtained for 100 realizations of a 50-hour CTAO observation.

3.3.3 PKS 2153-69

The HE spectrum of PKS 2153-69 was modeled using a log-parabola representation, with spectral index $\alpha \approx 2.36$ and curvature parameter $\beta \approx -0.16$. The presence of curvature in the spectrum, together with the marginal Fermi-LAT detection of the source, introduces additional uncertainties in the extrapolation to CTAO energies, since the spectral shape at TeV energies is poorly constrained by the available data.

Figure 3.7 shows the comparison between the modeled spectrum and the CTAO sensitivity for a 100-hour observation. The intrinsic flux lies below the CTAO sensitivity curve over most of the energy range, indicating that PKS 2153-69 is unlikely to be detected by CTAO with a standard 50-hour exposure. Unlike for IC 1531 and NGC 315, EBL absorption was not included in the analysis of this source, since the marginal HE detection already places the predicted TeV flux below the sensitivity limit. The simulated counts distribution (Figure 3.8) confirms a non-significant detection within the assumed exposure. Despite this negative outcome, PKS 2153-69 remains an interesting target for monitoring observations, particularly during potential flaring states, given its prominent jet activity, its FR II morphology, and its very large visibility from CTAO South at high zenith angles.

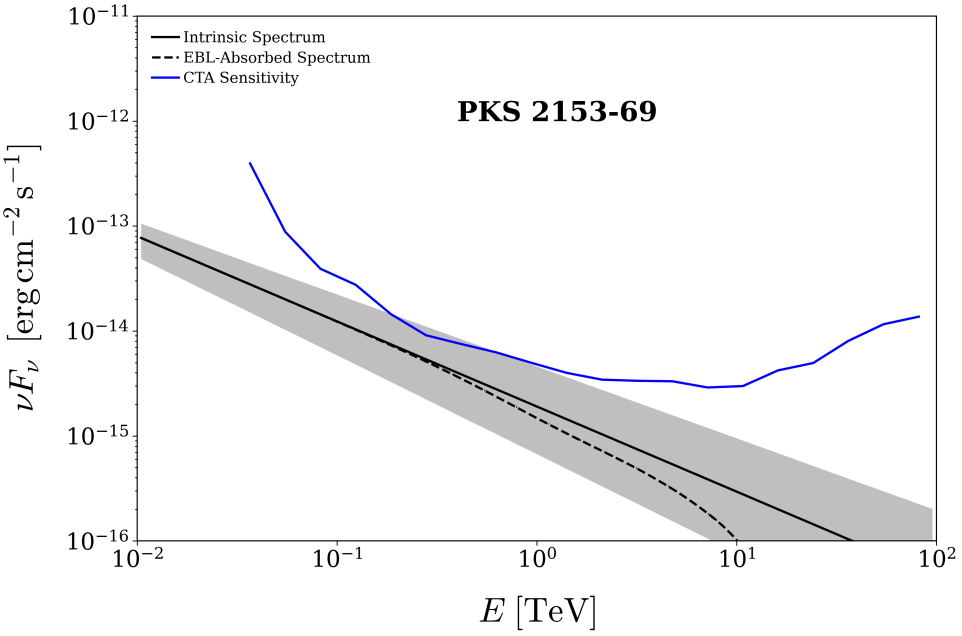

Figure 3.7: Energy-dependent differential flux sensitivity and model predictions for the PKS 2153-69 region. The black solid line represents the intrinsic extrapolated spectrum, and the blue line shows the CTAO sensitivity curve for a 100-hour observation. EBL absorption was not included in the analysis of this source.

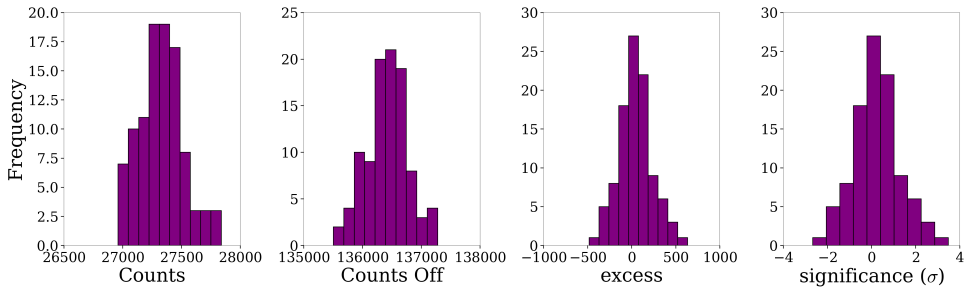

Figure 3.8: Distribution of simulated ON counts, OFF counts, excess counts, and detection significance (Eq. 3.6) for the PKS 2153-69 region, obtained for 100 realizations of a 100-hour CTAO observation.

3.4 Global Discussion and Summary

The combination of the comparative analysis of Section 3.2 and the source-by-source assessment of Section 3.3 provides a coherent picture of the CTAO detectability prospects of the three selected radio galaxies. Despite their similar HE spectral indices and their common classification as misaligned AGNs, the three sources show substantially different detection prospects, driven by the interplay between intrinsic flux, spectral shape, source confusion, EBL attenuation, visibility conditions, and exposure time.

IC 1531 and NGC 315 emerge as the most promising targets for CTAO observations. Both sources display power-law HE spectra with hard indices and intrinsic fluxes that approach or exceed the CTAO sensitivity curve in the sub-TeV range for a standard 50-hour exposure. NGC 315 benefits from a particularly clean γ-ray environment, with a single positionally coincident counterpart in the Fermi-LAT catalog, which reduces the systematic uncertainties of the analysis and supports a robust detection prospect with CTAO North. IC 1531, while located in a slightly more complex region with two catalogued counterparts within the ROI, exhibits a stronger intrinsic flux and benefits from the very high visibility from CTAO South. In both cases, the EBL absorption becomes relevant above a few hundred GeV and shapes the detectable energy range.

PKS 2153-69 represents a more challenging case. The marginal Fermi-LAT detection, combined with the spectral curvature inferred from the log-parabola fit, leads to a predicted CTAO flux below the standard sensitivity threshold for a 50-hour exposure. For this reason, the detectability of this source was evaluated assuming a longer exposure of 100 hours, which improves the integrated sensitivity by approximately a factor of $\sqrt{2}$ and allows a more meaningful assessment of the predicted flux. Even with this extended exposure, the detection prospects of PKS 2153-69 remain marginal, but the analysis indicates that long-duration observations represent a viable strategy to probe the high-energy emission of this source. The very large visibility from CTAO South at high zenith angles, together with the prominent jet activity and the FR II morphology of the source, further motivates the inclusion of PKS 2153-69 in future monitoring programs, particularly in connection with potential flaring states or future improvements in the analysis pipeline.

The methodology adopted in this chapter, which combines spectral information from Fermi-

LAT, counterpart association via *FeuPy*, visibility analysis from the CTAO arrays, and sensitivity comparison via *Gammapy*, provides a self-consistent framework for the detectability assessment of extragalactic γ-ray emitters in the VHE regime. The results indicate that nearby misaligned AGNs constitute a promising population for the early operations of CTAO, and that the geographic complementarity between the North and South arrays is a key element to ensure full-sky coverage of the radio galaxy population. The use of different exposure times across the sample, namely 50 hours for IC 1531 and NGC 315 and 100 hours for PKS 2153-69, reflects the diversity of intrinsic flux levels of misaligned AGNs and highlights the importance of tailoring the observation strategy to the specific properties of each target. The combination of SED modeling (Chapter 2) and CTAO detectability analysis (this chapter) offers a powerful approach to investigate the role of nearby radio galaxies as candidate γ-ray and multi-messenger sources, with direct implications for our understanding of particle acceleration in relativistic jets.

Chapter 4

Conclusions and Future Work

This chapter summarizes the main outcomes of the dissertation, emphasizes the principal conclusions of the analyses developed in Chapters 2 and 3, discusses the limitations of the adopted methodology, and outlines possible directions for future investigations. The discussion is organized into four sections: a summary of the results obtained throughout the work, the main physical and observational conclusions, an honest assessment of the limitations of the modeling approach, and a set of perspectives for future research.

4.1 Summary of Results

The central goal of this dissertation was to contribute to the understanding of the broadband emission and the detectability prospects of three nearby radio galaxies, namely IC 1531, NGC 315, and PKS 2153-69, all selected from the catalog of [24] based on their low redshift ($z < 0.03$). These sources, classified as MAGNs, constitute valuable laboratories for the study of non-thermal emission processes in relativistic jets, since their intrinsic emission is not dominated by the strong Doppler boosting characteristic of blazars. The work combined two complementary analyses, namely the SED modeling of the broadband emission of each source within a one-zone leptonic framework, and the detectability assessment of the same sources in the VHE regime with the next-generation CTAO.

In Chapter 1, a general overview of active galactic nuclei was presented, with particular

emphasis on the structural and emission properties of radio galaxies. The chapter introduced the main morphological elements of AGNs, the Fanaroff-Riley classification scheme, the distinction between high- and low-excitation radio galaxies, and the unified model that links the different observational classes within a common physical framework. The role of nearby radio galaxies as candidate γ-ray emitters and as plausible sources of UHECRs and astrophysical neutrinos was also discussed, providing the broader scientific context of the dissertation.

In Chapter 2, the broadband SEDs of the three sources were modeled using the *JetSeT* numerical package within a one-zone leptonic scenario. The analysis used updated multiwavelength datasets compiled through the *Firmamento* platform [46], which combine recent catalog data and observations not available in earlier SED studies of these sources. The modeling included a phenomenological pre-fitting stage, a Minuit-based optimization, and an MCMC exploration of the parameter space. The three sources display the characteristic double-peaked SED of non-thermal jet sources, with the low-energy component well reproduced by synchrotron emission and the high-energy component accounted for by the SSC mechanism. The inferred physical conditions of the emitting regions, including the magnetic field strength, the radius of the emitting region, the bulk Lorentz factor, the viewing angle, and the parameters of the broken power-law electron energy distribution, were derived for each source and compared with previous studies available in the literature [19, 18].

In Chapter 3, the HE component of the SED was extended to the VHE regime in order to evaluate the detectability of the three sources with CTAO. The methodology, based on the *Gammapy* library [28] and the *FeuPy* framework, included the construction of regions of interest, the identification of γ-ray counterparts from the Fermi-LAT 3FGL and 4FGL catalogs [29], the modeling of the HE spectra using power-law and log-parabola parametrizations, the computation of source visibility from the two CTAO arrays, and the simulation of ON/OFF observations to evaluate the detection significance via the Li & Ma formula. The analysis also included the effect of Extragalactic Background Light (EBL) absorption for IC 1531 and NGC 315, using the EBL model of [23].

4.2 Main Conclusions

The combined results of the SED modeling and the CTAO detectability analysis lead to a coherent picture of the broadband emission and the observational prospects of the three selected radio galaxies. The main conclusions of the dissertation can be summarized as follows.

The one-zone leptonic scenario provides an acceptable description of the broadband emission of IC 1531, NGC 315, and PKS 2153-69, with the SSC mechanism reproducing the high-energy peak in all three cases. This finding supports a common non-thermal origin of the radiation, dominated by relativistic electrons in the jets, despite the differences in morphological class (FR I for IC 1531 and NGC 315, FR II for PKS 2153-69) and in excitation regime (LERG for IC 1531 and NGC 315, HERG for PKS 2153-69) of the sources.

The inferred physical conditions of the emitting regions reveal substantial differences between the sources. IC 1531 is found to be strongly particle-dominated, with $U_e/U_B \sim 25$, indicating a non-equipartition regime that may reflect efficient particle acceleration or intrinsic limitations of the one-zone approach. NGC 315 and PKS 2153-69 show milder departures from equipartition, with $U_e/U_B \sim 3$ and $U_e/U_B \sim 1.5$, respectively, consistent with more balanced energy budgets between particles and magnetic field. The break Lorentz factors γ_b span roughly one order of magnitude across the sample, while the spectral steepenings $\Delta\alpha = \alpha_1 - \alpha$ across all three sources align closely with physical radiative expectations (ranging from $\Delta\alpha \approx 0.83$ in NGC 315 to $\Delta\alpha \approx 1.45$ in PKS 2153-69 and $\Delta\alpha \approx 1.74$ in IC 1531), consistent with standard synchrotron cooling and acceleration processes.

The comparison with previous studies shows that the leptonic SED modeling of nearby radio galaxies suffers from significant parameter degeneracies, but also that the inclusion of new multiwavelength data leads to non-negligible refinements of the inferred physical parameters. The case of NGC 315 is particularly illustrative, since our solution and that of [18] describe substantially different physical scenarios, namely a strongly boosted nearly aligned jet in our case and a mildly relativistic misaligned jet in theirs, while still providing acceptable fits to the broadband data. This dichotomy reinforces the well-known difficulty of constraining simultaneously the Doppler factor, the bulk Lorentz factor, and the viewing angle from SED modeling alone, and highlights the importance of complementary observational constraints, such as VLBI kinematics or independent estimates of the jet inclination.

In the VHE regime, the three sources display significantly different detection prospects with CTAO. IC 1531 and NGC 315 emerge as the most promising targets, with intrinsic fluxes that approach or exceed the CTAO sensitivity curve in the sub-TeV range for a standard 50-hour exposure. NGC 315 benefits from a particularly clean γ-ray environment, with a single positionally coincident Fermi-LAT counterpart, while IC 1531 exhibits a stronger intrinsic flux and a very high visibility from CTAO South. PKS 2153-69, on the other hand, presents a more challenging case, with a marginal Fermi-LAT detection, evidence of spectral curvature, and a predicted CTAO flux below the standard sensitivity threshold for a 50-hour exposure. For this reason, the detectability of this source was evaluated assuming an extended exposure of 100 hours, which improves the integrated sensitivity and allows a more meaningful assessment of its emission, although the detection prospects remain marginal even with this longer integration. The prominent jet activity of the source, its FR II morphology, and its very large visibility from CTAO South nevertheless motivate its inclusion in future monitoring programs, particularly in connection with potential flaring states.

The detectability analysis also illustrates the geographic complementarity between the CTAO North and South arrays. IC 1531 and PKS 2153-69 are preferentially observable from CTAO South, while NGC 315 is best suited for observations from CTAO North. The use of different exposure times across the sample, namely 50 hours for IC 1531 and NGC 315 and 100 hours for PKS 2153-69, reflects the diversity of intrinsic flux levels of misaligned AGNs and highlights the importance of tailoring the observation strategy to the specific properties of each target. This complementarity, together with the inclusion of EBL absorption effects in the spectral modeling, indicates that nearby misaligned AGNs constitute a promising population for the early operations of CTAO and that the dual-site design of the observatory is a key element to ensure full-sky coverage of the radio galaxy population.

4.3 Limitations of the Methodology

Despite the satisfactory description provided by the leptonic one-zone framework, the methodology adopted in this dissertation presents several limitations that should be considered when interpreting the results. These limitations are inherent to the simplifying assumptions of the model and to the available observational data, and they offer concrete directions for future im-

provements.

The first limitation concerns the one-zone assumption itself. By construction, this approach attributes the entire broadband emission to a single, homogeneous region within the jet, ignoring the possible spatial complexity of the emitting plasma. In several of the analyzed sources, the transition region between the synchrotron and SSC components of the SED is not fully reproduced by the model, suggesting that multi-zone scenarios or structured jet configurations may be required to provide a more accurate description of the emission. In addition, the assumed homogeneous geometry does not capture energy-dependent escape, transport, or cooling effects that are likely to operate in real jets.

The second limitation is associated with parameter degeneracies. The SED modeling involves a large number of free parameters, several of which are not independently constrained by the available data. In particular, the simultaneous determination of the Doppler factor, the bulk Lorentz factor, and the viewing angle is well known to be degenerate when the available data do not include independent constraints from VLBI observations or variability information. The comparison with the work of [18] for NGC 315 provides a clear illustration of this degeneracy, since two substantially different physical configurations can produce comparable fits to the broadband data. The MCMC exploration carried out in this work confirms that, in some sources, the high-energy spectral index reaches the boundary of the explored parameter space, indicating that its inferred value should be interpreted with caution.

The third limitation refers to the restriction to purely leptonic processes. Although leptonic models are sufficient to describe the broadband emission of the three sources within the achieved level of precision, hadronic and lepto-hadronic mechanisms may also contribute, particularly at the highest energies. These processes are of special interest in the context of multi-messenger astrophysics, since they predict associated neutrino emission, but they were not included in the present work due to the additional free parameters they would require and the limited observational constraints currently available for the three sources.

The fourth limitation concerns the VHE detectability analysis. The extrapolation of the HE spectra to the energy range covered by CTAO is performed using parametric models fitted to Fermi-LAT data, which extends only up to a few hundred GeV. The behavior of the spectra at TeV energies is therefore poorly constrained, particularly in the case of PKS 2153-69, where the marginal Fermi-LAT detection and the inferred spectral curvature introduce significant uncertainties in the predicted CTAO flux. In addition, EBL absorption was included for IC 1531

and NGC 315 but not for PKS 2153-69, which limits the comparability of the detectability assessments across the three sources.

Finally, the analysis does not incorporate the time variability of the sources. Although radio galaxies are generally less variable than blazars, multi-epoch observations could reveal flux changes that are not captured by the time-averaged SEDs used in this work, and that could affect the detectability prospects with CTAO, especially during transient or flaring states.

4.4 Future Work

The analyses developed in this dissertation open several directions for future investigations, addressing both the modeling of the broadband emission and the observational prospects of the selected sources.

A natural extension of the present work is the implementation of more sophisticated emission scenarios, including multi-zone leptonic models and lepto-hadronic frameworks. Multi-zone models could provide a more accurate description of the transition region between the synchrotron and SSC components, while lepto-hadronic scenarios would allow a self-consistent treatment of the role of relativistic protons in the high-energy emission and an estimate of the associated neutrino fluxes. Recent works have demonstrated the relevance of such approaches in the context of TeV blazars and high-synchrotron-peaked BL Lacs [10, 16], and similar methodologies could be applied to the present sample to investigate the role of misaligned AGNs as multi-messenger sources.

The inclusion of new multiwavelength observations would also significantly improve the analyses presented in this dissertation. In particular, dedicated VLBI observations would provide independent constraints on the jet inclination and the apparent superluminal motion of the parsec-scale jets, helping to break the degeneracy between the Doppler factor, the bulk Lorentz factor, and the viewing angle. Multi-epoch X-ray observations, for example with NuSTAR or with future instruments such as Athena, would offer additional constraints on the high-energy electron population, while updated Fermi-LAT analyses could refine the HE spectra of the sources, particularly in the case of PKS 2153-69, where the current detection is marginal.

The detectability analysis with CTAO can also be extended in several directions. The inclusion of EBL absorption effects for PKS 2153-69, the simulation of longer exposure times, and the

consideration of source variability would provide a more complete assessment of the observational prospects of this source. In addition, the methodology developed in Chapter 3 can be applied to larger samples of nearby radio galaxies, providing population studies that complement the case-by-case analyses carried out here. The combination of CTAO observations with multi-messenger facilities such as IceCube-Gen2 and the future SWGO array will also be of particular interest, since misaligned AGNs are among the candidate sources of high-energy astrophysical neutrinos.

Finally, the present analysis can also be connected to the broader question of the origin of UHECRs. Nearby radio galaxies, given their proximity below the GZK horizon [5, 6] and their powerful jets, are commonly invoked as plausible accelerators of cosmic rays up to the highest observed energies. The development of self-consistent multi-messenger models for the three sources analyzed in this dissertation, combining SED modeling, neutrino predictions, and cosmic-ray propagation, represents a promising line of research that builds directly on the framework established in this work.

In conclusion, the dissertation has provided an updated and self-consistent description of the broadband emission and the CTAO detectability prospects of IC 1531, NGC 315, and PKS 2153-69, contributing to the broader effort of characterizing nearby misaligned AGNs as multi-messenger sources. The combination of theoretical modeling, multiwavelength data analysis, and detectability simulations with next-generation facilities offers a promising path toward a deeper understanding of relativistic jets, non-thermal particle acceleration, and the physical processes governing active galactic nuclei in the local Universe.

Appendix A

Corner plots

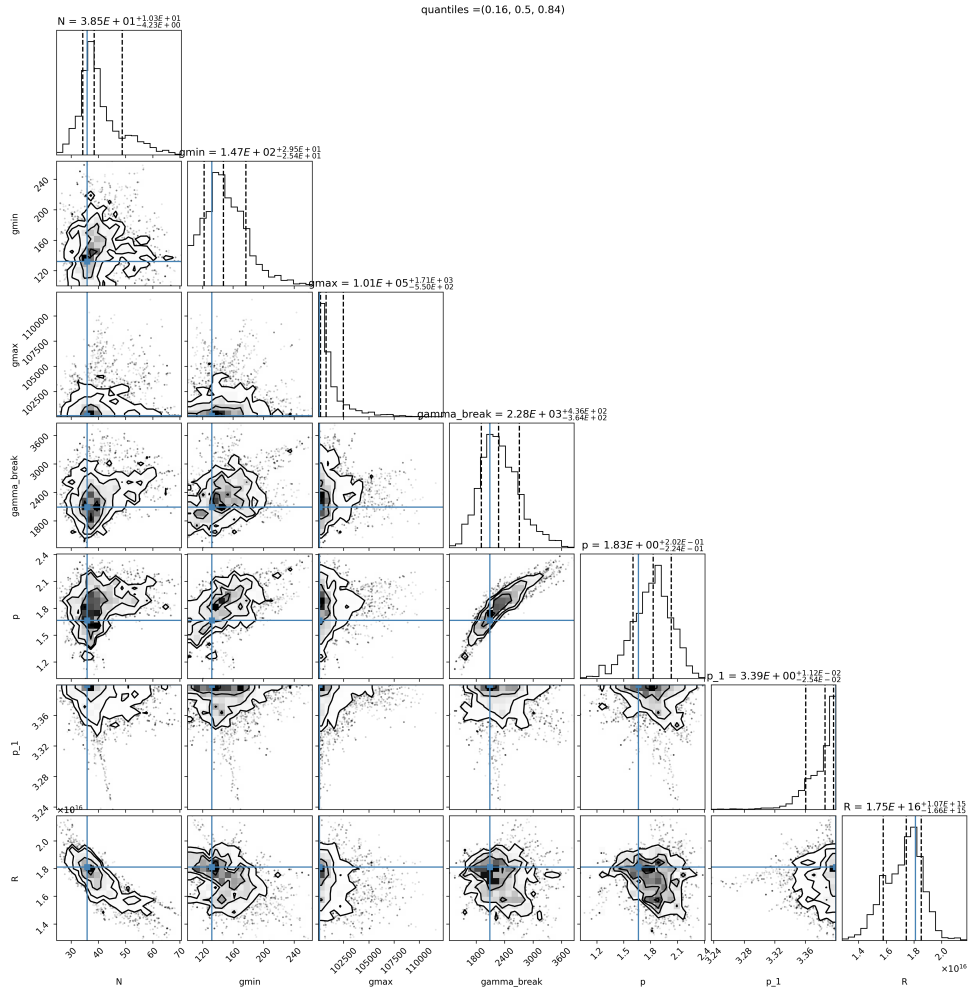

Figure A.1: Corner plot for the SED modelization of IC 1531.

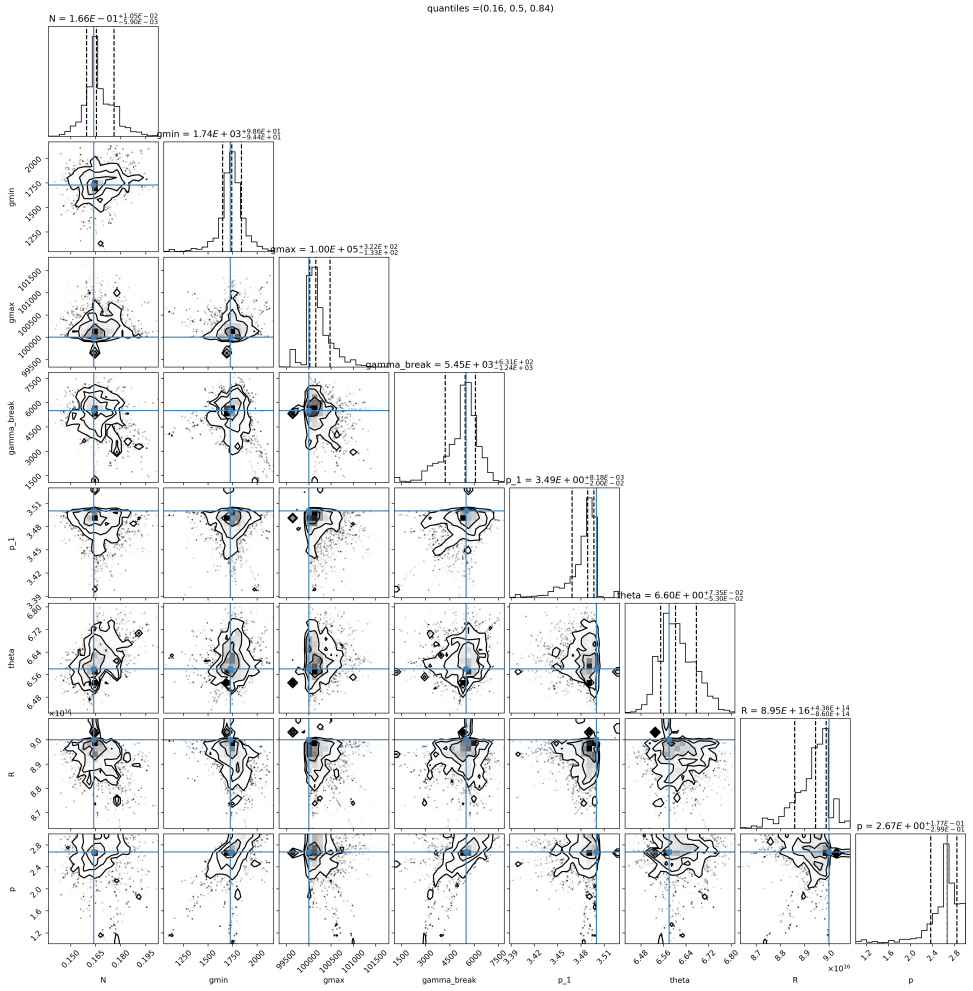

Figure A.2: Corner plot for the SED modelization of NGC 315.

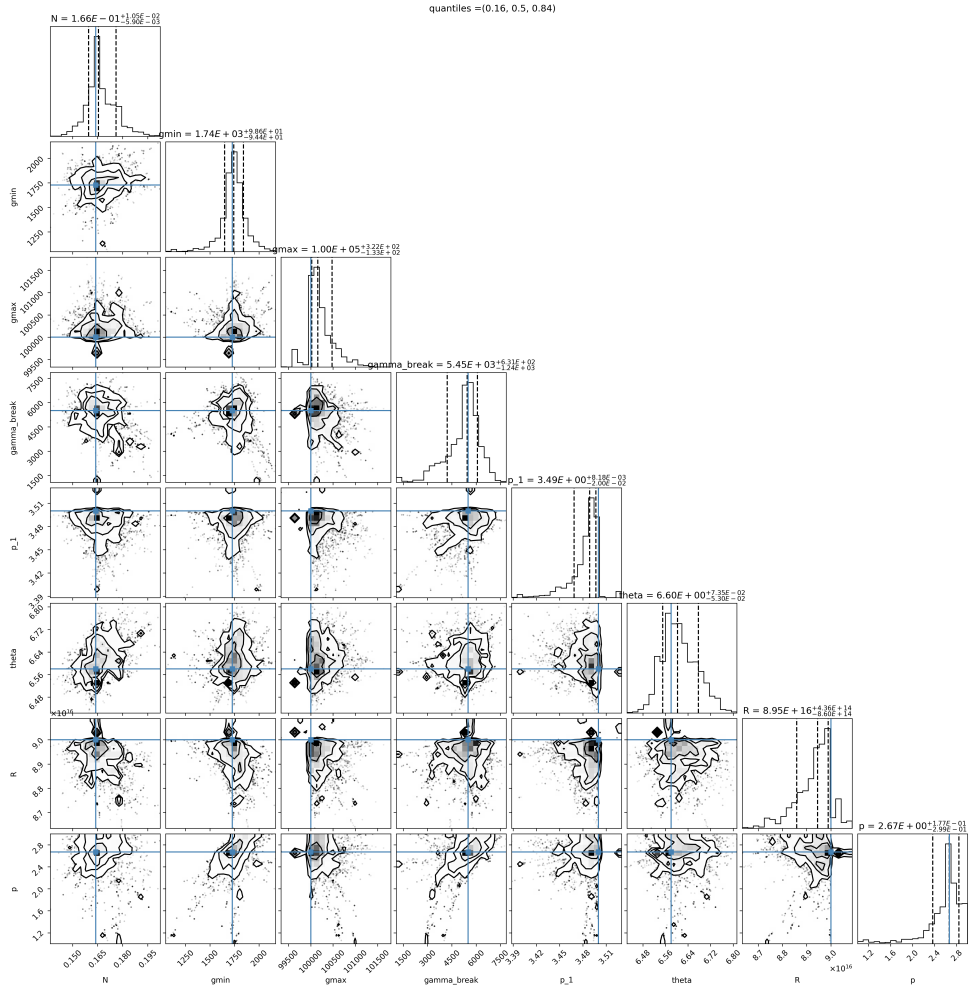

Figure A.3: Corner plot for the SED modelization of PKS 2153-69.

Bibliography

[1] H. Netzer, *The Physics and Evolution of Active Galactic Nuclei*, Cambridge University Press (2013).

[2] C. M. Urry and P. Padovani, *Unified Schemes for Radio-Loud Active Galactic Nuclei*, Publications of the Astronomical Society of the Pacific **107**, 803 (1995).

[3] P. Padovani et al., *Active galactic nuclei, what's in a name?*, Astronomy and Astrophysics Review **25**, 2 (2017).

[4] M. J. Hardcastle and J. H. Croston, *Radio galaxies and feedback from AGN jets*, New Astronomy Reviews **88**, 101539 (2020).

[5] K. Greisen, *End to the Cosmic-Ray Spectrum?*, Physical Review Letters **16**, 748 (1966).

[6] G. T. Zatsepin and V. A. Kuzmin, *Upper Limit of the Spectrum of Cosmic Rays*, JETP Letters **4**, 78 (1966).

[7] IceCube Collaboration et al., *Multimessenger observations of a flaring blazar coincident with high-energy neutrino IceCube-170922A*, Science **361**, eaat1378 (2018).

[8] M. Böttcher et al., *Leptonic and Hadronic Modeling of Blazars*, ApJ (2013).

[9] G. Ghisellini, *Radiative Processes in High Energy Astrophysics*, lecture notes, INAF – Osservatorio Astronomico di Brera (2024).

[10] S. V. Bernardo da Silva, L. A. Stuani Pereira, and R. C. dos Anjos, *Bethe-Heitler Cascades and Hard Gamma-Ray Spectra in Flaring TeV Blazars: 1ES 0414+009 and 1ES 1959+650*, Universe **11**, 177 (2025).

[11] A. Tramacere, *JetSeT: Numerical modeling and SED fitting tool for relativistic jets* (2020).

[12] A. Tramacere et al., *Stochastic Acceleration and the Evolution of Spectral Distributions in Synchro-Self-Compton Sources: A Self-consistent Modeling of Blazars' Flares* (2011).

[13] A. Tramacere et al., *Swift observations of the very intense flaring activity of Mrk 421 during 2006. I. Phenomenological picture of electron acceleration and predictions for MeV/GeV emission* (2009).

[14] F. M. Rieger, *An Introduction to Particle Acceleration in Shearing Flows*, Galaxies **7**, 78 (2019).

[15] G. Madejski and M. Sikora, *Gamma-Ray Observations of Active Galactic Nuclei*, Annual Review of Astronomy and Astrophysics **54**, 725 (2016).

[16] L. A. Stuani Pereira and R. C. dos Anjos, *High-Synchrotron-Peaked BL Lacs as Multi-Messenger Sources: Connecting Ultra-High-Energy Cosmic Rays and Neutrinos*, Galaxies **14**, 40 (2026).

[17] Cherenkov Telescope Array Consortium, *Science with the Cherenkov Telescope Array*, World Scientific Publishing (2019).

[18] R. de Menezes et al., *Gamma-ray observations of low-luminosity active galactic nuclei*, Monthly Notices of the Royal Astronomical Society (2020).

[19] A. De Rosa et al., *Faint γ-ray sources at low-redshift: the radio galaxy IC 1531*, Monthly Notices of the Royal Astronomical Society (2017).

[20] N. Fraija et al., *Blazar Jets and Prospects for TeV–PeV Neutrinos and Gamma Rays Through Cosmic-Ray Interactions*, The Astrophysical Journal (2016).

[21] R. Sasse, R. P. Costa Jr., L. A. Stuani Pereira, and R. C. dos Anjos, *Blazars Jets and Prospects for TeV-PeV Neutrinos and Gamma Rays Through Cosmic-Ray Interactions*, Brazilian Journal of Physics **55**, 60 (2025).

[22] A. Franceschini, G. Rodighiero, and M. Vaccari, *Extragalactic optical-infrared background radiation, its time evolution and the cosmic photon-photon opacity*, Astronomy & Astrophysics **487**, 837 (2008).

[23] A. Domínguez et al., *Extragalactic background light inferred from AEGIS galaxy-SED-type fractions*, Monthly Notices of the Royal Astronomical Society **410**, 2556 (2011).

[24] Y. Chen et al., The Astrophysical Journal Supplement Series **265**, 60 (2023).

[25] A. J. Young, A. S. Wilson, S. J. Tingay, and S. Heinz, *The halo, hot spots and jet/cloud interaction of PKS 2153-69*, The Astrophysical Journal (2005).

[26] Y.-W. Yu and J. Zhang, *Hard X-ray view of two γ-ray-detected low-luminosity active galactic nuclei: NGC 315 and NGC 4261*, Astronomy & Astrophysics (2025).

[27] B. Ananthamoorthy et al., *Enhanced UV emission knot in the giant radio galaxy NGC 315: Hint of patchy star formation?* (2024).

[28] A. Donath et al., *Gammapy: A Python package for gamma-ray astronomy*, Astronomy & Astrophysics **678**, A157 (2023).

[29] S. Abdollahi et al. (Fermi-LAT Collaboration), *Fermi Large Area Telescope Fourth Source Catalog*, The Astrophysical Journal Supplement Series **247**, 33 (2020).

[30] J. E. Thorne, *Lighting the Night: The Spectral Energy Distributions of Galaxies*, Ph.D. thesis, University of Western Australia (2023).

[31] L. Pfeiffer, *Leptonic modelling of the candidate neutrino emitter blazar 5BZB J1150+2417*, Master's thesis, Julius-Maximilians University Würzburg (2024).

[32] M. C. Weisskopf, H. D. Tananbaum, L. P. Van Speybroeck, and S. L. O'Dell, *Chandra X-Ray Observatory (CXO): overview*, Publications of the Astronomical Society of the Pacific **114**, 1 (2002).

[33] F. Jansen, D. Lumb, B. Altieri, J. Clavel, M. Ehle, C. Erd, D. Gabriel, M. Guainazzi, E. Gondoin, R. Much, et al., *XMM-Newton observatory. I. The spacecraft and operations*, Astronomy & Astrophysics **365**, L1 (2001).

[34] F. A. Harrison, W. W. Craig, F. E. Christensen, C. J. Hailey, W. W. Zhang, S. E. Boggs, D. Stern, C. M. Cook, K. Forster, P. Giommi, et al., *The Nuclear Spectroscopic Telescope Array (NuSTAR) High-Energy X-Ray Mission*, The Astrophysical Journal **770**, 103 (2013).

[35] W. B. Atwood, A. A. Abdo, M. Ackermann, W. Althouse, W. Anderson, M. Axelsson, L. Baldini, J. Ballet, G. Barbiellini, D. Bastieri, et al., *The Large Area Telescope on the Fermi Gamma-ray Space Telescope Mission*, The Astrophysical Journal **697**, 1071 (2009).

[36] J. L. E. Dreyer, *Index Catalogue of Nebulae Found in the Years 1888–1894*, Memoirs of the Royal Astronomical Society **51**, 185 (1895).

[37] J. L. E. Dreyer, *Second Index Catalogue of Nebulae and Clusters of Stars*, Memoirs of the Royal Astronomical Society **59**, 105 (1908).

[38] T. Bassi, G. Migliori, P. Grandi, C. Vignali, M. A. Pérez-Torres, R. D. Baldi, E. Torresi, A. Siemiginowska, and C. Stanghellini, *Faint γ-ray sources at low redshift: the radio galaxy IC 1531*, Monthly Notices of the Royal Astronomical Society **481**, 5236 (2018).

[39] J. L. E. Dreyer, *A New General Catalogue of Nebulae and Clusters of Stars*, Memoirs of the Royal Astronomical Society **49**, 1 (1888).

[40] R. Morganti, A. B. Peck, T. A. Oosterloo, G. van Moorsel, A. Capetti, R. Fanti, P. Parma, and H. R. de Ruiter, *Is cold gas fuelling the radio galaxy NGC 315?*, Astronomy & Astrophysics **505**, 559 (2009).

[41] J. G. Bolton, F. F. Gardner, and M. B. Mackey, *The Parkes Catalogue of Radio Sources, Declination Zone $-20°$ to $-60°$*, Australian Journal of Physics **17**, 340 (1964).

[42] R. A. E. Fosbury, R. Morganti, W. Wilson, R. D. Ekers, S. di Serego Alighieri, and C. N. Tadhunter, *Radio jet interactions in the radio galaxy PKS 2152-699*, Monthly Notices of the Royal Astronomical Society **296**, 701 (1998).

[43] The Astropy Collaboration, A. M. Price-Whelan, B. M. Sipőcz, H. M. Günther, P. L. Lim, S. M. Crawford, S. Conseil, D. L. Shupe, R. L. Craig, N. Dencheva, et al., *The Astropy Project: Building an Open-science Project and Status of the v2.0 Core Package*, The Astronomical Journal **156**, 123 (2018).

[44] P. Virtanen, R. Gommers, T. E. Oliphant, M. Haberland, T. Reddy, D. Cournapeau, E. Burovski, P. Peterson, W. Weckesser, et al., *SciPy 1.0: Fundamental Algorithms for Scientific Computing in Python*, Nature Methods **17**, 261 (2020).

[45] D. Foreman-Mackey, D. W. Hogg, D. Lang, and J. Goodman, *emcee: The MCMC Hammer*, Publications of the Astronomical Society of the Pacific **125**, 306 (2013).

[46] D. Tripathi, P. Giommi, A. Di Giovanni et al., *Firmamento: A Multimessenger Astronomy Tool for Citizen and Professional Scientists*, The Astronomical Journal **167**, 116 (2024).

[47] T.-P. Li and Y.-Q. Ma, *Analysis methods for results in gamma-ray astronomy*, The Astrophysical Journal **272**, 317 (1983).